# Fabrication and Characterization of Piezoelectric Thin Films on Si Wafers and Fibers

Inauguraldissertation

Zur

Erlangung der Würde eines Doktors der Philosophie
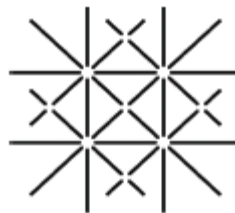
vorgelegt der

Philosophisch-Naturwissenschaftlichen Fakultät

der Universität Basel

von

Ratnesh Thapliyal

aus Indien

**UNI BASEL**

EMPA Dübendorf, 2009

Genehmigt von der Philosophisch-Naturwissenschaftlichen Fakultat

auf Antrag der Herren Professoren:

Prof. Dr. H. J. Hug

Prof. Dr. E. Meyer


Basel, den 11, December 2007

Prof. Dr. Hans-Peter Hauri, Dekan

*Dedicated to my parents*

# Abstract

Ferroelectric films are very promising materials in many areas of modern technologies such as microactuators, microtransducers, sensors and phase modulators. The application area of ferroelectric films is growing due to the need for miniaturization and integration of electronic components. Ferroelectric films have several advantages over bulk material, such as smaller size, less weight, easier integration to integrated circuit technology, lower operating voltage, higher speed, and the ability to fabricate micro-level structures. Lead Zirconate Titanate (PZT) film is an appropriate candidate for the above mentioned applications due to it's excellent piezoelectric properties.

The principal aim of this study is the optimization of PZT film deposition process parameters on Si wafers using a single metallic PZT target. The optimized process parameters for wafers are transferred to the PZT coating on fiber substrates, showing good flexibility and high tensile strength. The objective is to investigate the piezo properties of the PZT coated fibers for sensor application.

PZT thin films have been deposited by pulsed DC sputtering process on Ti/Pt/Ti coated Si wafers. The influence of various processing parameters (substrate temperature, oxygen partial pressure, annealing conditions) on the

properties of PZT films have been studied. It has been found that $490^0$C is the optimum substrate temperature to obtain crystalline and homogeneous films with excellent adhesion. The deposited films have been processed by conventional annealing (CA) and rapid thermal annealing (RTA) to obtain pure pervoskite phase. Different crystallographic orientations have been observed for different annealing procedures (110 for CA and 111 for RTA) for films deposited at low $O_2$ partial pressure. In order to investigate the depth profile, a novel GD−OES method has been developed. The obtained results revealed deficiency of oxygen within the pervoskite structure.

Using higher oxygen partial pressure within the plasma and adequate post annealing methods (CA and RTA) results in pure PZT pervoskite structure. Hardness and Young's modulus of these oxygen rich samples are almost three times higher than the oxygen deficient films, indicating a improved crystallization in oxygen rich samples. CA and RTA processed films repeatedly show different crystallographic orientations (100 for CA and 110 for RTA). Annealed samples show dense and multi−crystalline structure with grain sizes in the range of 100 to 300 nm. Depth analysis revealed constant elemental concentrations close to the target value. It has been found that CA processed samples show higher polarization and remanence than RTA processed samples because of larger grain sizes and different polarization axis. CA and RTA processed samples have 100 and 110 polarization axis. Grains can be easily polarized in 100 direction compare to the hard 110 direction, results in higher polarizations.

The optimized process parameters have been used for PZT deposition on Gold/glassfiber, steel fiber and copper fiber. Some modification of parameters were essential due to following reasons: different substrate geometry, different sticking of Ti atoms on the fiber surface, oxidation of fiber surfaces

and temperature distribution through the fibers. RTA processing at $650^0$C has been found the best optimum temperature to obtain pervoskite structure. All the coated fibers revealed (110) preferred orientation. A dense and crystalline structure has been observed on Gold/glassfibers and on steel fibers. Grain sizes are in the range of 100 to 400 nm range. Some micro cracks have been observed on steel and Cu fibers, due to large difference in thermal expansion coefficients between PZT and substrates. Atomic concentration of Pb, Zr, Ti and O atoms have been found in stoichiometric ratio and close to our target value.

PZT coated steel fibers have been investigated as force sensors. Sensor sensitivity and piezoelectric coefficient, $d_{31}$ has been found to be 1.95 V/N and 870 pm/V, which is comparable to the literature value (500 pm/V on wafers from multi target).

# Acknowledgments

I would like to thank all the people with whom I spent a wonderful time throughout my dissertation.

First, I would like to thank Prof. Dr. Hans— Josef Hug for giving me an opportunity to do my PhD under his supervision, who aided me in more ways than I could ever recount here. It has been a great pleasure to discuss with Hans. Those deliberations provided me with the deep insight of Physics.

I am very grateful to Prof. Dr. Ernst Meyer for kindly accepting to be a referee on my thesis.

I would also like to thank Prof. Dr. Hans—Joachim Güntherodt showing his interest in this dissertation.

I am personally grateful to Dr. Fortunato Giuseppino for supervising me as a local advisor for my PhD thesis at EMPA St Gallen.

I would also like to thanks all the current and previous dear members of the Plasma group for assisting me for my work and creating pleasant working atmosphere. I would also like to thank my department "Advance fiber" for helping me to conclude my thesis, successfully.

I would also like to thank Dr. Peter Kappenberger for AFM, Dr. Patrick Schwaller for GDOES, and Aude Pelisson for XRD measurements.

# Contents

# List of Tables

# List of Figures

# 1

# Introduction

This thesis covers the fabrication and characterization of piezoelectric lead zirconate titanate (PZT) thin films on wafers and on fibers from single target sputtering process. The properties of piezo−electric and ferroelectric materials are presented in this chapter to provide the foundation, necessary for understanding the results of this research.

## 1.1   Piezoelectricity

Piezoelectricity is the property of some materials to exhibit electric polarization when subjected to mechanical stress. Conversely, if an electric field

is applied to a piezoelectric material a stretching or compressing process is observed depending upon the orientation of the applied field. The word "piezo" is derived from the Greek word "piezein", which means to squeeze or press. The piezoelectric effect was discovered in quartz in 1880 by Pierre and Jacques Curie [1].

```
              ┌─────────────────┐
              │ 32 Crystal Classes │
              └─────────────────┘
        ┌──────────────┴──────────────┐
┌────────────────┐           ┌──────────────────┐
│ 11 Classes     │           │ 21 Classes       │
│ Centrosymmetric│           │ Non-Centrosymmetric│
└────────────────┘           └──────────────────┘
                    ┌──────────────┴──────────────┐
              ┌────────────────┐         ┌──────────────────┐
              │ 1 Classes      │         │ 20 Classes       │
              │ Non piezoelectric│       │ Piezoelectric    │
              └────────────────┘         └──────────────────┘
                           ┌──────────────┴──────────────┐
                     ┌────────────────┐         ┌──────────────────┐
                     │ 10 Classes     │         │ 10 Classes       │
                     │ Non pyroelectric│        │ Pyroelectric     │
                     └────────────────┘         └──────────────────┘
                                    ┌──────────────┴──────────────┐
                              ┌────────────────┐         ┌──────────────────┐
                              │ Non Ferroelectric│       │ Ferroelectric    │
                              └────────────────┘         └──────────────────┘
```
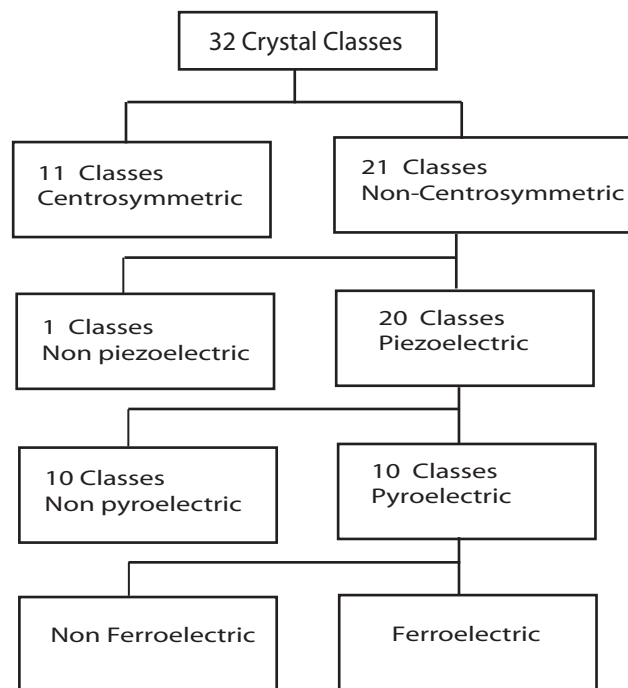
*Fig. 1.1:* Classification of the crystal systems

Out of the 32 crystal classes, 21 lack a center of symmetry(Fig.1.1). A centrosymmetric crystal does not possess polar properties, and cannot be piezoelectric. Out of the 21 non centrosymmetric classes, 20 are piezoelectric. Ten of these piezoelectric classes are also pyroelectric. Pyroelectric materials have a spontaneous polarization which depends on the temperature and exists in the absence of an applied electric field or stress. This polarization is result

of a displacement between the centers of positive and negative charges in the crystal unit cell and changes when the material is heated uniformly causing a charge to develop on the surface.

## 1.2   Mathematical description of piezoelectricity

In this section, mathematical description of piezoelectricity is provided to lay the framework of characterization of piezoelectric material. To begin, let us consider the first law of thermodynamics, which gives the energy of a system as

$$dU = TdS + EdD + \theta d\sigma \tag{1.1}$$

where U is the energy, T the stress, S the strain, E the electric field, D the electric displacement, $\theta$ temperature and $\sigma$ the entropy of the system [2, 3, 4]. In equation 1.1, the first term (TdS) is the work done per unit volume when strains are changed by small amounts, the second term (EdD) is the electrical work done on a system, and the last term ($\theta d\sigma$) represents the amount of heat generated when the system undergoes a change (from the second law of thermodynamics). Transformation of variables can be affected by means of Legendre transformations and the consequential scalar function is called a thermodynamic potential. The thermodynamic potential $\phi$, a form of the Gibbs free energy, is defined as:

$$\phi = U - TS - ED - \theta d\sigma \tag{1.2}$$

Neglecting the temperature and entropy, differentiating equation 1.2 and combining it with equation 1.1, yields

$$d\phi = -SdT - DdE \tag{1.3}$$

Since $\phi$ is a function of state (all quantities on the right side are functions which define the state of the system), we can write:

$$d\phi = \frac{\delta\phi}{\delta T}dT + \frac{\delta\phi}{\delta E}dE \tag{1.4}$$

Hence, comparing equation 1.4 and 1.3, we can get:

$$\frac{\delta\phi}{\delta T} = -S, \frac{\delta\phi}{\delta E} = -D \tag{1.5}$$

and the differentials of S and D may be written as,

$$dS = \frac{\delta S}{\delta E}dE + \frac{\delta S}{\delta T}dT \tag{1.6}$$

$$dD = \frac{\delta D}{\delta E}dE + \frac{\delta D}{\delta T}dT \tag{1.7}$$

Therefore, using Einstein summing convention, with indices ranging from 1 to 3 the equation of state of piezoelectricity can be written as :

$$S_{ij} = d_{mij}E_m + S_{ijkl}T_{kl} \tag{1.8}$$

$$D_i = \epsilon_{im}E_m + d_{ikl} \tag{1.9}$$

The indices indicate the crystallographic unit vectors $x_1$, $x_2$, and $x_3$. Note that $d_{mij}$ and $d_{ikl}$ are the linear piezoelectric strain coefficients, $s_{ijkl}$ is the linear elastic compliance and $\epsilon_{im}$ is the linear dielectric permitivity [5]. These quantities are defined by the partial derivatives in equations 1.6 and 1.7. $T_{kl}$ and $E_m$ are the independent variables in these equations.

The above equations can be written in the form of polarization as follows:

$$P_n = \chi_{mn}E_m + d_{nkl}T_{kl} \tag{1.10}$$

which shows that polarization ($P_n$) is a function of an electric field ($E_m$) with proportionality constant $\chi_{mn}$, the susceptibility, and stress ($T_{kl}$) with proportionality constant $d_{nkl}$, the piezoelectric constant.

## 1.3   Ferroelectricity

Ferroelectric materials are a subset of pyroelectrics, which are in turn, a subset of the piezoelectric. Ferroelectric materials possess a spontaneous electric dipole moment [6, 7, 8]. These materials develop charges, when subjected to stress and change their shape, when subjected to an electric field. In contrast to pyroelectric materials, ferroelectrics have a switchable spontaneous polarization. Ferroelectric materials generally exhibit ferroelectric behavior below a certain temperature and paraelectric behavior above this temperature, called Curie temperature [9, 10]. At the Curie temperature structural phase transition occurs from a high-temperature non ferroelectric paraelectric phase to a low-temperature ferroelectric phase. Typically, a ferroelectric material in the paraelectric phase is centrosymmetric, which means it is not polar. Lead zirconium titanate (PZT) is a cubic above the Curie temperature, which shows neither pyroelectric nor piezoelectric behavior. Below the Curie temperature PZT has many phases, depending on the Ti and Zr atomic concentrations.

## 1.4   Ferroelectric domains and hysteresis loop

Ferroelectric materials possess regions with uniform polarization called ferroelectric domains. Within a domain, all the electric dipoles are aligned in

the same direction. There may be many domains in a crystal separated by interfaces called domain walls. A ferroelectric single crystal, when grown, has multiple ferroelectric domains. A single domain can be obtained by domain wall motion which is possible only by the application of an appropriate electric field. A very strong field could lead to the reversal of the polarization in the domain, known as domain switching [11]. The main difference between pyroelectric and ferroelectric materials is that the direction of the spontaneous polarization in ferroelectrics can be switched by an applied electric field, whereas in pyroelectric polarization is not reversible. The inversion of polarization can be observed by measuring the ferroelectric hysteresis as shown in Fig.1.2



*Fig. 1.2:* Typical hysteresis loop of ferroelectric material

As the electric field strength is increased, the domains start to align in the positive direction giving rise to a rapid increase in the polarization (OB). At

very high electric field, the polarization reaches a saturation value ($P_s$). The polarization does not fall to zero when the external field is removed. At zero external field, some of the domains remain aligned in the positive direction, hence the crystal will show a remnant polarization $P_r$. The crystal cannot be completely depolarized until a field of magnitude OF is applied in the negative direction. The external field required to reduce the polarization to zero is called the coercive field strength $E_c$. If the field is increased to a more negative value, the direction of polarization flips and hence a hysteresis loop is obtained. The value of the spontaneous polarization $P_s$ (OE) is obtained by extrapolating the curve onto the polarization axes (CE). The polarization continues to increase with the increase of applied field even beyond the field required to obtain $P_s$. This is because all of the domains are oriented parallel to each other [5]. However the individual $TiO_6$ polarizable units can continue to be distorted increasing the polarization. This is an important contrast to ferromagnetic material where application of a magnetic field greater than required for $M_s$ does not increase the net magnetic moment of the material [12].

## 1.5   Lead zirconate titanate (PZT)

PZT is a solid solution of lead titanate ($PbTiO_3$) and lead zirconate ($PbZrO_3$). Fig.1.3 shows the phase diagram of PZT. The cubic perovskite unit cell (named after the mineral perovskite, CaTiO3) is shown in Fig.1.4 and has a general chemical formula $ABO_3$.

The excellent ferroelectric behavior of materials with the perovskite crystal structure is thought to be related to the mobility of the small B cation within the oxygen octahedron. This behavior can be characterized by a tolerance factor "t" that is defined by the following relation:
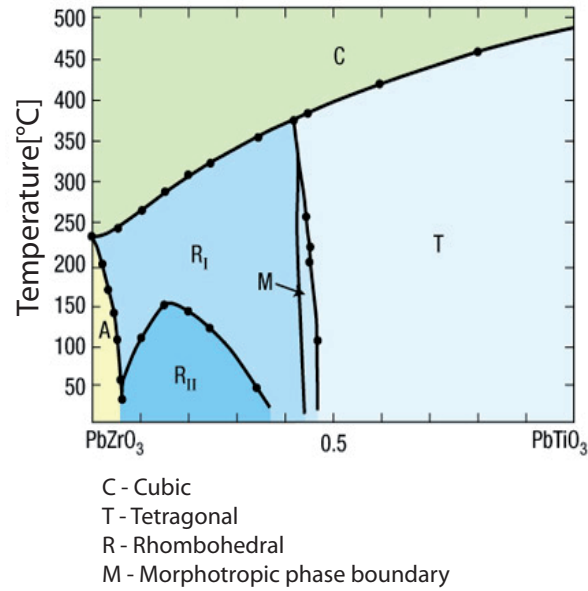
*Fig. 1.3:* Phase diagram of the solid solution system of $PbTiO_3$ - $PbZrO_3$
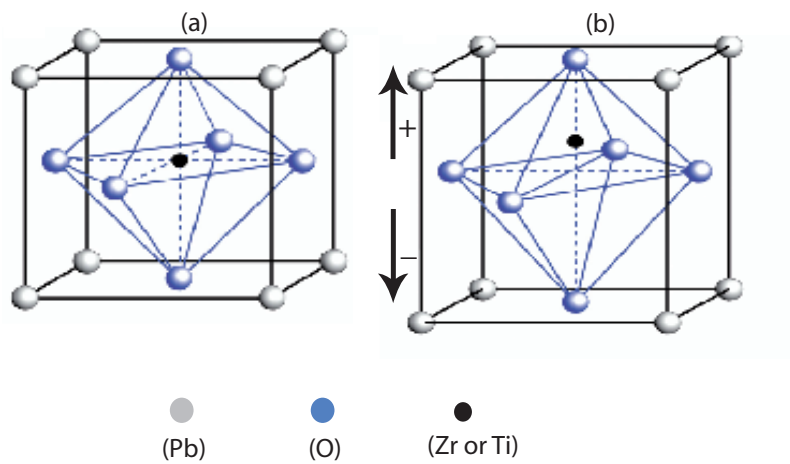


*Fig. 1.4:* PZT unit cell:(a) Perovskite-type lead zirconate titanate (PZT) unit cell in the symmetric cubic state above the Curie temperature, (b) Tetragonally distorted unit cell below the Curie temperature.

$$t = (R_A + R_O)/\sqrt{2}(R_B + R_O) \tag{1.11}$$

where $R_A$ is the radius of the ion in the Pb (A) position, $R_o$ the radius of an oxygen anion, and $R_B$ the radius of the ion in the central (B) position. A tolerance factor, "t", between 0.95 and 1.0 implies that the central (B) ion fits in the oxygen octahedron and results in cubic perovskite structure. A tolerance factor "t" greater than unity indicates the space for the central (B) ion is too large, which is free to move around [7]. Crystal structures, where "t" is larger than 1.0 typically, exhibit ferroelectric behavior, whereas those with a tolerance factor lesser than 0.95 are non ferroelectric. PZT has several ferroelectric phases that are all slightly deviated from the cubic structure. In the cubic perovskite structure, Pb atoms occupy the corners of a cube, with O atoms at the face centers and a Zr or Ti atom at the center of the unit cell. The tetragonally distorted perovskite structure (shown in Fig.1.4) is distorted along the polarization direction with Pb atoms at the corners of the tetragonal and the Zr/Ti atoms are displaced from the center. As shown in the phase diagram for PZT (Fig.1.3), the Curie point varies from $230^0$C to $490^0$C depending upon the Zr/Ti ratio. The ferroelectric phase is tetragonal for high Ti concentrations, and rhombohedral for high Zr concentrations. In the tetragonal case, the Zr and Ti atoms displace off the center towards any of the six oxygen atoms (in a cubic $< 100 >$ direction) and the Pb and O atoms shift as well. In the rhombohedral case, the Zr and Ti atoms are displaced towards the center of one of the eight faces of the oxygen octahedral (in a cubic $< 111 >$ direction). Maximum values of the dielectric and piezoelectric properties are observed in the composition at the boundary between the rhombohedral and tetragonal phase, called morphotropic phase boundary (MPB) [13]. The MPB separating the two ferroelectric tetragonal

and orthorhombic phases has a composition with a Zr/Ti ratio of $\approx 52/48$. The poling of the PZT ceramic is also easy at this composition because the spontaneous polarization within each grain can be switched to one of the 14 possible orientations (eight [111] directions for the rhombohedral phase and six [100] directions for the tetragonal phase) [14].

## 1.6 Plasma and their properties

Plasma is an ionized gas, into which sufficient energy is provided to generate free electrons from atoms or molecules and to allow ions and electrons to coexist. Langmuir was the first to use the term "plasma" in 1929 to describe the inner region of an electrical discharge [15]. Later the definition was broadened to define a state of matter, i.e. "ionized gas", in which a significant number of atoms or molecules are electrically charged or ionized, and it is referred to as the fourth state of matter [16, 17]. An ionized gas consists of equal numbers of positive and negative charges. Chen et al. gave the definition of the plasma state "plasma is a quasi-neutral gas of charged particles which exhibit a collective behavior" [18]. In the case of man-made plasma, an electric field is applied between a metal electrode and the outer plasma reactor. Electrons eject from the electrode into the gas within the reactor. These highly energetic electrons collide with the gas atoms to form ions and free electrons. Excitation, relaxation, ionization and recombination are the essential mechanisms in the plasma. The collisions with energetic particles readily move atoms and ions from their ground energetic level to an excited energetic level. The excited states atoms relax back to their ground levels by emitting light in the form of photons, thus, plasma is a visible glow. Plasma is an electrical conductor. The dominant charge carriers in the processing plasma are the electrons. Because of their low mass, electrons respond much

faster to electric field than the heavier ions, hence they can respond quicker to the local change in potential. The plasma potential can perturb over a certain distance, known as self shielding or Debye length. The Debye length can be obtained by solving Poisson's equation in one dimension and given (in cm) as follows:

$$\lambda_d = \sqrt{\frac{kT\epsilon_0}{n_e e^2}} \tag{1.12}$$

Where $\epsilon_0$ is the permittivity of free space, kT the electron kinetic energy, $n_0$ the number of electron density and e the electronic charge, respectively [19]. The Debye length describes the attenuation of plasma potential in the plasma. Over a distance x, the potential reduces by 1/e of the initial value [20]. The concentration of the charged particles in between of the Debye length, $N_d$ is given as:

$$N_d = n_0 \left( \frac{4\pi\lambda_d^3}{3} \right) \tag{1.13}$$

If $N_d < 1$, collective phenomena are of little importance and the plasma consists of an "independent particle", indicating that collisions dominate. If $N_d \gg 1$, relevant number of particles are collectively responsible for the Debye cloud, revealing a "collective behavior". This collective effect dominates over collisions, which is an essential criterion of plasma.

When plasma is perturbed from neutrality, large number of restoring forces strive to reestablish the charge neutrality. Because of the mass difference between ions and electrons, electrons will respond first to the restoring forces. These restoring forces are proportional to the displacement, which is a condition for oscillations. The restoring force can be given by Hook's law

$$F = -kx \tag{1.14}$$

where, x is the displacement of electrons and k is the spring constant of this oscillation system. Since the electrons have inertia, the system behaves as a harmonic oscillator and the electrons overshoot and oscillate around the equilibrium position. This is known as plasma frequency $\omega_d$:

$$\omega_d = (n_o e^2 / \epsilon_o kT) \tag{1.15}$$

Collision of the electrons with other species in the plasma will eventually damp out this oscillatory motion. Below the plasma frequency, electrons can move to shield the charges or potential imbalance created by the applied electric field. Electrons in the plasma don't respond quickly enough to shield the applied field at the frequency higher than plasma frequency.

The electron energy distribution in the plasma is given by the Maxwellian distribution:

$$f_\epsilon = 2\sqrt{\epsilon/\Pi})(kT)^{3/2}e^{-\epsilon/kT} \tag{1.16}$$

Where $\epsilon$ is the electron energy, k the Boltzmann's constant and T the temperature. The average kinetic energy of the electrons is given by:

$$E_{av} = (3/2)kT \tag{1.17}$$

The equation above shows that the temperature is directly proportional to the kinetic energy of the particles. The electron energy in a plasma is typically in the range of 1 to 10 eV.

## 1.7 *Plasma in the presence of a magnetic field*

Plasmas are moderately conductive and therefore weakly perturbed by the application of an electric fields. A moving charge in a magnetic field is a subject of force $F_m$ represented as:

$$F_m = q.\vec{v} \times B \tag{1.18}$$

Where q is the charge of the particles, v the velocity and B the magnetic field. This force produces an acceleration that is inversely proportional to the mass of the charge species, hence only electrons are affected, as ions have too large mass. For charged particles moving at right angles to the magnetic field, this force causes the particles to move in an orbital path. The radius of this orbit can be found by equating the magnetic and centripetal forces [21]

$$r = mv_\perp/qB \tag{1.19}$$

$$r = mvsin\theta/qB \tag{1.20}$$

Or it can be written in terms of the particles kinetic energy, KE as follows:

$$r = \sqrt{2m(KE)}/qB \tag{1.21}$$

The rotational frequency of a given particles in a magnetic field can be found as

$$w = qB/m \tag{1.22}$$

Where $\omega$ is the rotational speed in radiant/s. This frequency is also known as cyclotron frequency If motion of an electron is coupled with the velocity parallel (V $cos\theta$) to the magnetic field, general motion will be a helix. Hence in presence of magnetic field net velocity of the electrons reduces towards the reactor wall to zero, reducing wall recombination losses. A second effect of the helical path is to increase the total path length traveled by an electron on its way to anode. This creates more ionization and excitation.

In the absence of magnetic field conductivity is given by

$$\sigma = Ne^2/m_e v_e \tag{1.23}$$

Where $\nu_e$ is the collision frequency for electrons and ions, $m_e$ is the mass of an electron and $v_e$ is the velocity of an electron. When a magnetic field is applied to the plasma, the conductivity parallel to the magnetic field is the same as given in equation 1.25, but the conductivity parallel to the magnetic field is given by

$$\sigma = 1 + w/v_e^2 \tag{1.24}$$

## 1.8  Magnetron

If a magnetic field is oriented correctly, the E×B drift paths can be configured to form a closed loop or path. Thus, instead of loosing the drifting electron at one side of the plasma, they are effectively trapped near the cathode and form a drifting circulating current. This device is known as a magnetron. Fig.1.5 shows the schematic diagram of a circular planer magnetron device. The circular magnetron consists of a water cooled cathode surface backed by an array of magnets and electromagnets. Poles of the magnet are oriented such that the center exits of the device are the first pole and the annular ring at the edge of the cathode is the second. The magnetic fields of lines travel from central pole to the outer ring in a parabolic shape. They cut through the cathode surface near the poles and are approximately parallel to the surface of the cathode. The secondary electrons emitted from the cathode as a result of ion bombardment are constrained in this annular region, resulting in an increased ionization and much denser plasma.
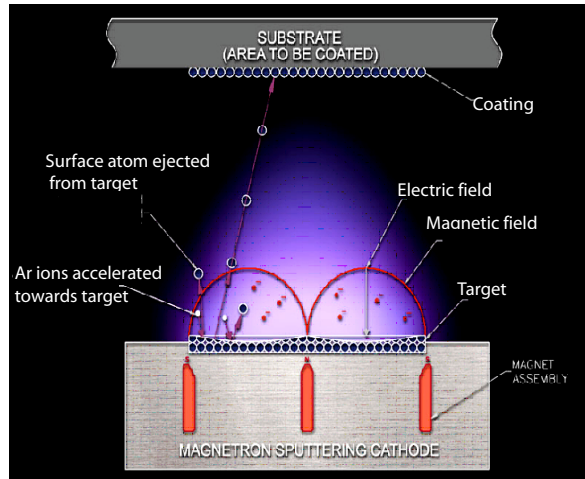
*Fig. 1.5:* Schematic diagram of sputtering process

## 1.9  Sputtering

Sputtering is a physical process whereby atoms in a solid target material are ejected due to the bombardment of the material by energetic ions. It is commonly used for thin-film deposition. Sputtering involves many interrelated physical and chemical processes. Sputtering is very well known technology for thin film deposition applied in many fields such as optical storage media [22], solar control [23], transparent conducting electrodes [24], VLSI [25], ICs etc. [26, 27, 28]. The main advantages of sputtering technologies are as follows

- Excellent film uniformity, particularly over large area

- Surface smoothness and thickness control

- Deposition of films with nearly bulk like properties

- Versatility - the sputter process is a kinetic process involving momentum exchange rather than a chemical or thermal process and therefore any material can be introduced into a gas discharge or sputtered from solid

- Good adhesion

- High deposition rate. The higher rate of deposition results in lower impurity incorporation because fewer atoms are able to reach the surface of the substrate in the same amount of time. Sputter sources for film deposition can be categorized in two ways:

  Glow discharge (diode, triode and magnetron)

  Ion beam

In all the cases the particles are ejected from the target by the mechanism of momentum exchange between energetic particles and surface atoms [29]. If we consider the mass of the incident atom is $m_i$ and the mass of the target atom is $m_t$, then energy transfer during the collision is given by

$$= 4m_i \times m_t/(m_i + m_t)^2 \qquad (1.25)$$

The sputtering process is the result of a series of such collisions [29]. There are several key factors of the sputtering process that affect the properties of the resulting films. These includes:

- The power supplied to the plasma

- The pressure of the plasma

- The type of gas used in the plasma

- The temperature of the substrate

- The system geometry

Of these, the geometry of the system has the most pronounced effect on the sputtering process. Atoms/molecules must traverse the distance between the target and the substrate, interacting with the species in the plasma, altering the distance of travel and the number of interaction events between the species of the plasma [30, 31]. The geometric relation between the target and substrate also affects the uniformity of the deposited films. A number of variations exist based on the basic sputtering process that have been used to improve it. The most common variation between sputtering processes is the type of electric field used to generate the plasma. Many sputter deposition processes use metallic targets with a DC voltage bias to generate the plasma [32, 33]. Sputtering of non-conductive targets typically requires the use of a RF power supply, which reduces the charge build up at the target [34, 35]. Fig.1.5 show the experimental setup of magnetron sputtering. It is also possible to fabricate ceramic films using a metallic target by introducing a reactive gas ($O_2$ or $N_2$) during the sputtering process. The atoms of the gas react with the metallic atoms at the surface of the target, or during their way through the plasma, forming a ceramic film on the substrate surface. PZT films have been fabricated by various sputtering method such as sputtering (RF, DC), pulsed DC sputtering etc [36]. In this thesis a novel pulsed DC magnetron sputtering method has been used to deposit PZT films on coated Si wafer and on different fiber substrates.

## 1.10   Pulsed DC sputtering

Magnetron sputtering is well known process widely used in industry but in the last decade, great attention has been devoted to the reactive pulsed dc

magnetron sputtering [37, 38]. The main aim of this effort is the reproducible fabrication of high-quality PZT films with a high deposition rate close to that of pure metal films. However in DC reactive magnetron sputtering continuous formation of oxide layer on the target results in target poisoning which leads to the accumulation of positive charges during the ion bombardment and consequently leads to arcing [39]. Pulsed DC magnetron sputtering is frequently used for reactive sputter deposition of dielectric film due to an ability to suppress the arcing, which leads to more stable process compared with dc magnetron sputter deposition. In pulsed DC magnetron process mid frequency ranging from 20-350 kHz is used [40].
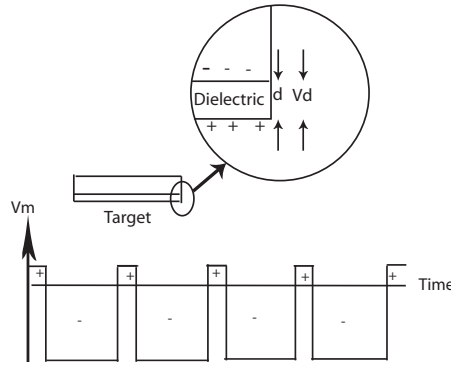


*Fig. 1.6:* Voltage pulse in pulsed dc magnetron device

In pulsed DC process the power is supplied using a high negative pulses interrupted by small positive pulses (see Fig.1.6). The dielectric layer is charged by positive ions causing voltage build up $V_d$, across the insulating layer with thickness d. Also the lower diagram shows the time dependent target voltage $V_m$ during the pulsed dc magnetron sputtering. In this way, charge at the oxide surface of the target may be neutralized by attracting electrons during the positive part of the cycle. It has been shown that properly matched positive and negative pulses lead to arc free reactive sputter deposition from pure metal target. In pulsed DC reactive sputtering erosion

of the target only takes place during the negative part of the duty cycle [41, 42]. Pulsed DC magnetron has been employed throughout the whole work presented in this thesis. It has been found that pulsed dc magnetron is a stable process without causing any arcing in target.

## 1.11 State of the art

During the last decade, much efforts have been spent on the miniaturisation of piezoelectric devices such as micro motors, micro positioners, and accelerometers. This led to promising progress in thin film technology, which mainly driven by research carried out on PZT thin films, makes this system promising for microelectro-mechanical systems (MEMS) and has therefore attracted great attention. New fields have arisen for the application of PZT coated substrate in the fiber form in sectors, such as Telecommunication, Textiles, Wireless energy harvesting etc. Modulation of the phase of light propagating inside the core of an optical fiber started in 1974 by Davies and Kinsley [43]. Costanitini et.al., Fox et.al and Sayer et.al made further contributions to improve the PZT coated optical fiber system for phase modulation by introducing PZT film processed by DC reactive magnetron sputtering process [44, 45, 46]. Researchers are currently working to implement PZT (pure or coated) fibers for industrial application [47, 48, 49, 50, 51]. Cass et.al , French et.al, Cai et.al. developed the pure PZT fibers by viscous solution technique, and sol−gel methods [52, 53]. H.Sato et.al made PZT fiber sensor by both hydrothermal method and extrusion method on Ti wire [54]. The main disadvantage of these PZT fibers are their low stability under mechanical stress. Most of these studies deal with chemical based solutions to provide pure PZT fibers or PZT coated fibers to improve the adhesion. Claude Muller studied in his thesis the PZT deposition on optical fibers by

reactive sputtering from multitarget PZT. These methods are not feasible for industrial purposes because of process limitations such as control of sputter rate of each target element individually, homogeneity of the films etc. There has been no reports on PZT coating on fibers from single PZT metallic target by pulsed DC sputtering process. However there is lack of knowledge with respect to PZT thin film deposition on fibers by single PZT target by sputtering process.

## 1.12   Aim of this work

The aim of this study is to establish the optimize processing properties for lead zirconate titanate (PZT) thin film by single target sputtering on wafers and fibers (both glass and metal ones) for sensor applications. There is still an insufficient knowledge base concerning the deposition parameters, coating on metal fibers, structural, chemical and electrical properties of coated fibers for sensor application. This technological kernel, from which PZT coated fiber sensor may originate. Following this objective, this study will concentrate on the followings aspects:

- Optimization of process parameter for PZT deposition on wafers from single PZT target via reactive sputtering

- Characterization of coated wafers to understand the influencing parameter with respect to structural, morphological, chemical and electrical properties. Special attention has been paid on annealing methods and influence of the oxygen concentrations. The analytical methods to be used are XRD, SEM, XPS, GDOES, Nano−indentation, AFM, Ferro-electric materials analyzer.

- Transforming the optimum process parameters obtained from PZT deposition on wafers to different fiber substrates.

- Characterization of the PZT coated fibers in the same manner as done on wafers.

- Build up of an instrumental setup to investigate the performance of the coated fibers as sensor with respect to sensitivity and piezo properties.

# 2

# Experimental methods and characterization tools

In this chapter, we will describe the necessary experimental requirement and their influence on the deposition of thin films such as target composition, substrate temperature, process parameter, annealing conditions. Detailed measured properties will be described in the chapter 3, 4, 5, 6 and 7. In the later part of this chapter brief description of the characterization tools used in this study is given.
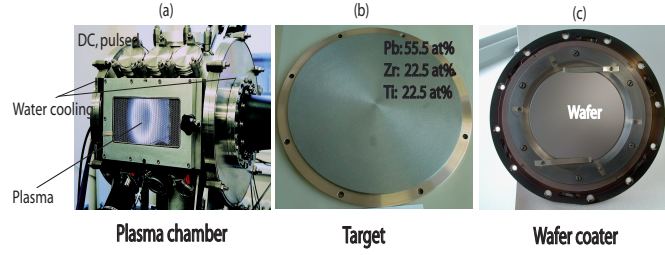
*Fig. 2.1:* Experimental set−up for thin film deposition: (a) plasma chamber, (b) sputtering target, (c) substrate holder for wafers

## 2.1   Target composition

For the sputtering process, target composition plays an important role, as sputter rates depends on the elements. In this thesis, PZT single metallic target has been used. This target (see Fig.2.1 (b)) has been provided by "Umicore Materials AG"

Target composition has the following atomic concentrations: (at%) Pb:55, Zr:22.5 and Ti:22.5. In order to compensate lead loss during the heating process and to obtain homogeneous and stoichiometric PZT films, 10% of excess Pb has been chosen in the target [55]. The atomic ratio of Zr and Ti for the target is 1:1 and the Pb/(Zr+Ti) ratio is 1.22 (excess lead). Since we use reactive sputtering, oxygen gas has been introduced into the chamber in addition to Ar gas during the process to get complete perovskite structure formation on the substrate. Having used the target for couple of years, it's composition has still remained constant. Hence, aging effects do not occur in this target and reproducibe properties of the films can be obtained over a long duration.

## 2.2   Substrate holder

In the case of wafer depositions, a substrate holder (Unaxis Balzers AG) (see Fig.2.1 (c)) has been used in the reactive chamber. The substrate holder was equipped with a cooling system to avoid any damage to interior materials attached with this holder. Each wafer, 8 inch diameter has been clamped by a spring to the surface of the substrate holder. The substrate has been heated to selected temperatures which were controlled by a temperature controller. A thermocouple has been attached to the substrate to ensure the stable thermal conditions.

## 2.3   Substrate structure

The principal substrate used throughout the studies is a $Si/SiO_2$ wafer coated with Ti/Pt/Ti metallization. Thicknesses of the layer sequences are Ti 6nm, Pt 140nm and Ti 40nm, respectively. The substrate or bottom electrode plays an important role for the PZT film deposition. Chen and Makenzie et.al. have studied qualitatively that the pervoskite formation is nucleation controlled [56, 57]. Hence transformation kinetics can be expedited when nucleation sites are created on the substrate [58]. Seeding layer provides large number of nucleation site on the substrate. Kumagai et al. revealed that seeding processes enhance the kinetics of crystallization of particles and encourages the formation of epitaxial film [59, 60].

In this study, Ti and Pt layer has been applied as a bottom electrode. Since PZT is deposited at high temperature in an oxidizing atmosphere to attain better electrical properties. Therefore the sequence of the layer beneath must be thermally stable and resistant to oxidation. Pt metal film has been used because it is relatively inert, thermally stable, has a high thermal con-

ductivity, is resistant to the oxidation and has a high schottky barrier height, which gives rise to a low leakage current density [61, 62]. Pure Pt film has weak adhesion to $SiO_2$, so that deposited PZT films easily peeled off after the deposition. $SiO_2$ is the barrier layer preventing contact between Pt and Si which could result in the formation of complex Pt silicide. The Ti layer is used to promote the adhesion layer between Pt and $SiO_2$ [63, 64, 65]. A very thin (6nm) Ti buffer layer has been applied on the top of $Pt/Ti/SiO_2/Si$ layer sequence. This Ti buffer layer on the Pt surface enhances the perovskite formation [66, 67]. Akoi et.al. showed the effect of Ti buffer layer on the crystallization process of PZT film. It has been shown that the nucleation temperature of PZT decreases with the presence of Ti buffer layer. This suggests that lead titanate (PTO) nuclei are generated first by reaction between Pb and Ti on the substrate (with Ti buffer layer), due to a lower crystallization temperature of lead titanate(PTO). Therefore the presence of thin Ti seeding layer leads to the formation of PZT at lower temperature [68].

## 2.4   Substrate temperature

It has been observed by various researchers that PZT thin films require high substrate temperature ranging from $450^0C$ to $650^0C$ [69]. Important factors are the control of the oxidation kinetics and the amount of the lead incorporated in the PZT film. Both are dependent on the substrate temperature. At higher substrate temperature atom diffusion at the interface between substrate and film can take place, leading to non-stoichiometric PZT composition. While low temperature deposition could avoid reaction and diffusion between film and the substrate [70]. In this study the substrate temperature has been varied from $430^0C$ to $510^0C$ for PZT deposition on coated Si wafers.

## 2.5   Process parameters

| Sputtering method | Pulsed DC Magnetron |
|---|---|
| Target composition (at%) | Pb(55)Zr(22.5)Ti(22.5) |
| Substrates | Si-wafer, layer sequence : Si/SiO$_2$/Ti(20nm)/Pt(140nm)/Ti(6nm) |
| Deposition temperature [$^0$C] | 510$^0$C, 490$^0$C, 460$^0$C, 430$^0$C |
| Gas flow during the process | Ar (60 sccm,10 sccm), O$_2$ (54 sccm, 90 sccm) |
| Post annealing temperature [$^0$C] CA and RTA process | 550 $^0$C, 600 $^0$C, 650 $^0$C and 700 $^0$C |
| Base pressure (mbar) | 2.0 * 10$^{-6}$ |
| Sputtering Gas Pressure (mbar) | 0.020 |
| Sputtering Power (W) | 250 |
| Frequency (kHz), Recovery time ($\mu$s) | 35 , 9 |
| Film thickness (nm) | 600, 1200 |

*Tab. 2.1:* Process parameters for PZT thin film deposition

- O$_2$ deficient - 54 sccm

- O$_2$ rich - 90 sccm

- CA: Conventional annealing

- RTA: Rapid thermal annealing

Table 2.1 shows typical process parameter of the PZT deposition on coated Si wafers. Prior to the PZT deposition, the plasma chamber was pumped down to a base pressure of 10$^{-6}$ mbar. A gas mixture of O$_2$ and Ar has been introduced into the chamber. In order to eliminate the contamination and to maintain the homogeneity of the target composition, a pre−sputtering in pure Ar atmosphere for 15 min has been performed. A shutter has been placed in front of the target for the prior target cleaning. PZT films have been deposited in pressure mode with the total pressure of

$20\mu$bar. Deposition rate of PZT films have been found to be 3.3 nm/min.

## 2.6    Annealing methods

Since annealing is an important step to get crystalline structure. PZT coated samples have been annealed by two different methods:

- CA: Conventional annealing

- RTA: Rapid thermal annealing
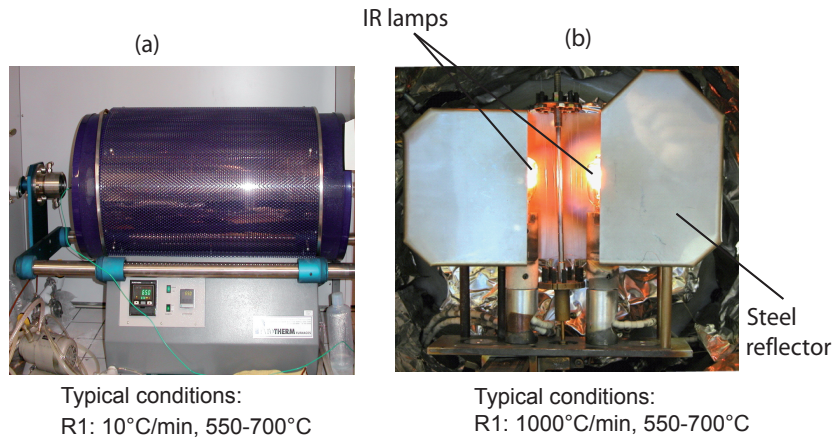


Fig. 2.2: Annealing methods: (a) Conventional annealing (CA), (b) Rapid thermal annealing (RTA)

Samples have been processed by CA in tubular furnace (Pyro Therm Furnace, Model no.14/75/500, see Fig.2.6) in air. All the samples are annealed at four different temperatures from $550^0$C, $600^0$C, $650^0$C and $700^0$C for 2 hrs respectively. Fig.2.3 (a) shows the typical heating ramp of the tubular furnace.

The rapid thermal annealing chamber has been built in the house by placing two IR lamps ( 5cm long) close to each other (see Fig.2.6). The IR
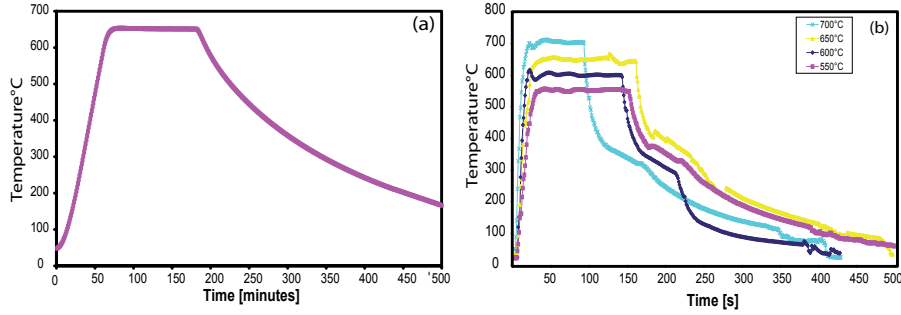
*Fig. 2.3:* Typical heating and cooling rate of CA and RTA processed samples: (a) Conventional annealing (CA), (b) Rapid thermal annealing (RTA)

lamps are surrounded by steel reflectors to prevent the heat loss. The RTA equipment is placed inside the same vacuum chamber as used for plasma deposition. Samples are annealed in vacuum at different temperatures from $550^0$C, $600^0$C and $650^0$C for 2 minutes and at $700^0$C for 1 minute respectively. Fig.2.3 (b) shows the Typical heating ramp of the RTA process.

## 2.7   Characterizations of the materials

In order to characterize PZT coated samples, a wide variety of methods are available nowadays. Within this study coated surfaces have been characterized by the thickness measurement, structural analysis (XRD), topographical analysis (SEM and AFM), elemental analysis (XPS and GDOES), electrical analysis (PE loop) and mechanical analysis (Nano−indentation) etc. Detailed analysis about these characteristics are given in next section.

## 2.8   Thickness measurement

Film thickness of the samples have been measured by the the Profilometer (KLA Tencor). In profilometry,the region of interest can be focused easily

by an optical microscope. Very thin (2.5 nm−1000 nm) step heights can be determined precisely as long as a suitable edge on the coated film is available. The process has an excellent repeatability and reproducibility. Fig.2.4 shows the typical thickness measurement performed on thin films.
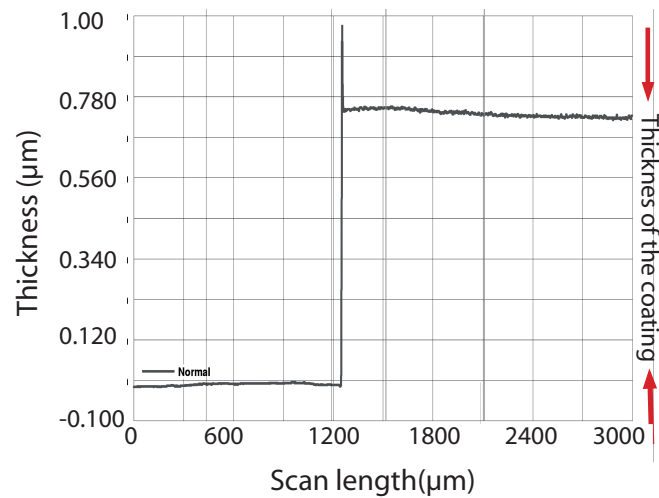


*Fig. 2.4:* Typical profile measured for a PZT coated sample

## 2.9   Structural investigations: XRD

The structure of the films were studied by X-ray diffraction (XRD) using a Philips Xpert MRD four-circle diffractometer. X-ray diffraction is a versatile, non destructive technique that reveals detailed informations about the crystallographic structure of different material. X-ray techniques are based on the elastic scattering of X-rays from structures that have long range order. Diffraction occurs as waves interact with a regular structure whose repeat distance is about the same as the wavelength. This phenomenon is common

in nature and occurs across a broad range of scales. X-rays have wavelength in the order of few $\mathring{A}$, the same as typical interatomic distance in crystalline solids. In 1912 W.L. Bragg gave a relationship between incident X-rays and angle of diffraction as follows:

$$n\lambda = 2dsin\theta \qquad (2.1)$$

where n is an integer, $\lambda$ is wavelength in $\mathring{A}$ (1.54$\mathring{A}$ for copper), d is interatomic spacing in $\mathring{A}$, $\theta$ is the diffraction angle in degrees [71, 72]

## 2.10   Surface morphology: Scanning electron microscopy (SEM)

Samples micro−structures have been investigated by scanning electron microscopy (Hitachi, S−4800). The SEM is an instrument that produces a largely magnified image by using electrons instead of light to form an image. A beam of electrons is produced at the top of the microscope by an electron gun. The electron beam follows a vertical path through the microscope, which is held within a vacuum. The beam travels through electromagnetic fields and lenses, which focus the beam down towards the sample. Once the beam has scanned the sample, electrons and X-rays are ejected from the sample. Detectors collect these X-rays, backscattered electrons, and secondary electrons and convert them into a signal, producing the final image.

## 2.11   Surface topography: AFM

The topography of plasma-coated surfaces have been characterized by atomic force microscopy (AFM) (commercial DI Dimension 3100 microscope) in a tapping mode. Si crystalline material has been used as a tip, which has

a resonance frequency = 223.6 KHz and Stiffness = 40 N/m. The basic concept of force microscopy is the measurement of forces between a sharp tip and a sample surface. Most commonly, the tip is mounted on the end of a cantilever which serves as a force sensor. Either the static deflection of the cantilever or the change in its dynamic properties due to tip sample forces can be exploited. A simple beam deflection system is used to monitor the cantilever displacement and measure cantilever deflection with a sub-angstrom resolution and its twisting angle. A laser beam is focused on the back side of the cantilever close to the tip position. The reflected laser beam is then entered onto the four quadrant photo diode. The signal regenerates on the piezo crystal. The tip is controlled by the piezo crystal. The movement of the piezo is recorded as a topographical picture by a computer. A typical system used for AFM analysis is illustrated in Fig.2.5.

Fig.2.6 shows the several operating mode of force microscopy. There are 3 regimes present, as a function of tip-to-sample separation distance, including contact, intermittent contact or tapping, and non-contact regimes, which are in fact different modes of AFM analysis.

For each of these regimes, the total attractive and repulsive forces differ. Contact mode force microscopy is based upon the static measurement of deflection of the cantilever. Topographic images are recorded by scanning the tip over the sample surface at constant cantilever deflection. The deflection corresponds to a normal force which can be calculated by multiplying spring constant. Detail description about the AFM is explicitly explained by Ernst Mayer, Hans Josef Hug, and Roland Bennewitz in the book "A lab on tip" [73].
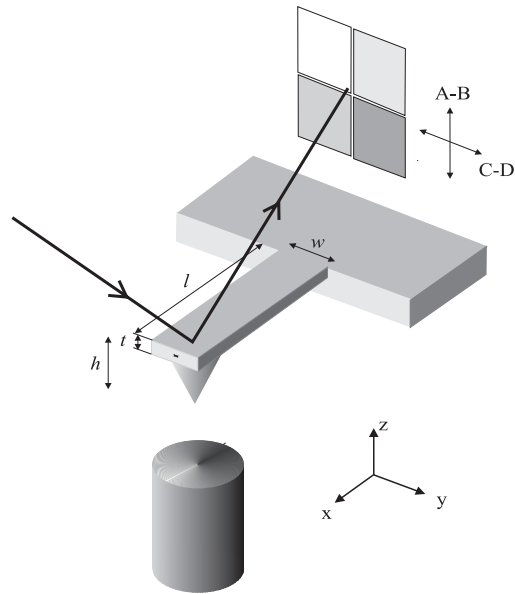
*Fig. 2.5:* Schematic diagram of the beam deflection. The relevant dimensions of the rectangular cantilever are indicated: length 'l', width 'w', thickness 't' and height of the tip 'h' (courtesy of Ernst Meyer, Hans Josef hug and Roland Bennewitz)
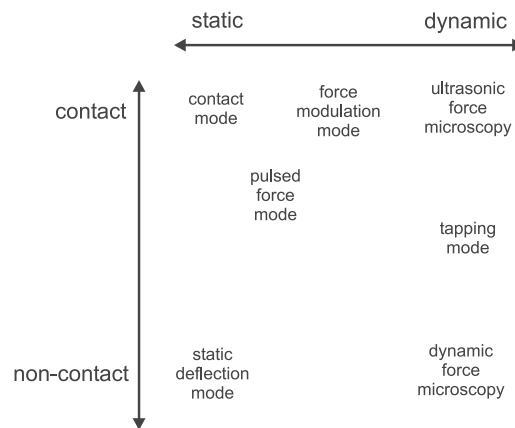


*Fig. 2.6:* Operation mode of force microscopy sorted with respect to static or dynamic detection and tip-sample contact formation.

## 2.12 Elemental Analysis: X−ray photoelectron spectroscopy (XPS)

XPS measurements have been performed using PHI LS 5600 instrument with standard MgK X-ray source. The energy resolution of the spectrometer was set at 0.8 eV/step at a pass energy of 187.85 eV for survey scans and 0.25 eV/step and 58.70 eV pass energy for region scans. The X-ray beam was operated at a current of 25 mA and an acceleration voltage of 13 kV. Charge effects were corrected using Carbon 1s = 285.0 eV. The concentrations of the surface species were determined using CasaXP software (peak areas using the instrument specific sensitivity factors).

XPS involves irradiation of a sample under vacuum by X−rays of known energy which caused photo ejection of electrons from atoms near the surface (Fig.2.7). The emitted electrons have a kinetic energy, which is given by following equation

$$KE = h\nu - BE - \phi_s \tag{2.2}$$
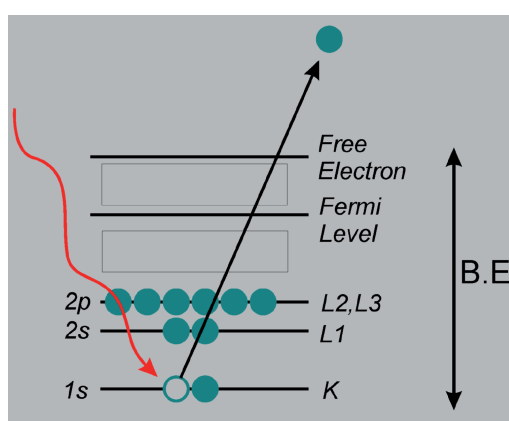


*Fig. 2.7:* Schematic diagram of X-ray photoelectron spectroscopy

where h$\nu$ is the energy of the photon, BE is the binding energy of the atomic orbital from which the electron originates and $\phi_s$ is the work function of the spectrometer. Each element has a characteristic binding energy, which can be used to identify the elemental composition of the sample substrate. Variation in the elemental binding energies (the chemical shift) arise from the difference in the chemical potential and polarizability of compounds. These chemical shifts can be used to identify the chemical state of the atoms being analyzed.

## 2.13   Depth analysis: Glow discharge optical emission spectroscopy (GDOES)

Depth profiling has been performed by GDOES (Instrument Type Jobin Yvon JY5000RF). In this method the sample is sputtered by Ar ions, whereas the sample represents the cathode itself. The atoms and ions sputtered from the sample interact with the species in the plasma and are transferred into various excited states. In the course of the subsequent de-excitation process, light emission with characteristic wavelengths for each element is analyzed in an optical spectrometer (see Fig.4.1).

More details about GDOES experiments and the data interpretation can be found in the literature [74, 75]. By this procedure depth profiles of several $\mu$m can be measured within a few minutes. This method is cheap because no expensive vacuum equipment, like that required for electron spectroscopy, is needed. Drawbacks of GDOES are incapability to perform micro spot analysis (typical sample area is about 13 mm$^2$) and the fact that the method is destructive (i.e. leaving a crater of 4 mm in diameter). The depth profiling process by GDOES can be divided in two parts. The first is the erosion of
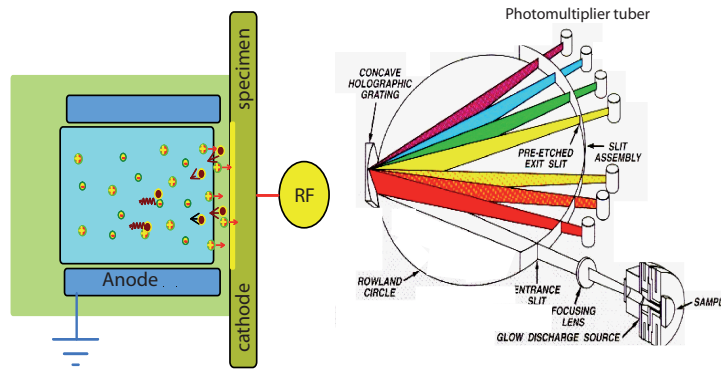
*Fig. 2.8:* Depth analysis by Glow-Discharge Optical Emission Spectroscopy (GD-OES)

material through bombardment with Ar ions, the second is the subsequent excitation of the sputtered material. Table 2.2 indicates the different parameter settings (Ar pressure, power, duty cycle). The pulse frequency has been kept fixed for all experiments at 5 kHz. The duty cycle indicates the time during which the plasma has been running for one half cycle of 100 $\mu$sec. A duty cycle of 0.125 therefore means that the plasma has been running for 12.5 $\mu$sec. Sputter rate for parameter set "d" is much higher than the rate for "a". It has been decided to use the parameters "a" for the quantitative measurements. This is due to the lower instantaneous power of "a" (45 W compared to 90 W for d) which induces less thermal stress in the sample.

## 2.14   Mechanical properties: Nano−indentation

In order to investigate the mechanical properties of the PZT coatings, nanoindentation measurements have been performed to determine the hardness and

*Tab. 2.2:* GD-OES parameters used for the depth analysis. The pulse frequency for all measurements was 5 kHz.

| Parameter set | Ar pressure (Pa) | Power (W) | Duty cycle | Sputtering rate(nm/s) |
|---|---|---|---|---|
| a | 600 | 45 | 0.125 | 1.0 |
| b | 600 | 45 | 0.500 | 6.6 |
| c | 800 | 45 | 0.125 | 1.1 |
| d | 600 | 90 | 0.125 | 3.0 |

the Young's modulus by MTS XP Nanoindenter. In a nanoindentation test, a diamond indentation tip is pressed into the sample surface. The applied load and the penetration depth into the surface are continuously measured during the loading and the unloading period [76, 77]. Load-displacement curves are analyzed by the Oliver and Pharr method, which allows calculating the sample hardness and the Young's modulus. Poisson number of 0.25 has been assumed for the calculation of the Young's modulus of the PZT coatings. For all measurements, a peak load of 1 mN has been applied on samples [78].

## 2.15   Electrical properties: PE loop

The Radiant Technologies (Precision LC, materials analyzer) standard ferroelectric tester has been used for the measurement of field induced polarization. The polarization hysteresis loop is obtained with the sawyer-tower circuit mode [8]. The sawyer-tower circuit is composed of a linear capacitor ($C_l$) connected with a integrating capacitor ($C_i$) (see Fig.2.9). Polarization is obtained by measuring the charge collected on the integrating capacitor. A triangular pulse of 1 kHz has been applied to all samples. Fields have been varied from 200 kV/cm to 1200 kV/cm to achieve the saturation polarization

of the PZT thin films.
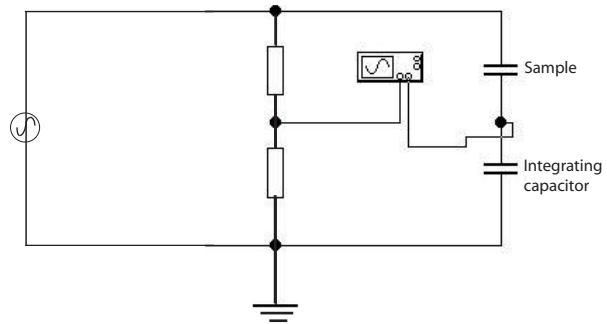


*Fig. 2.9:* Schematic diagram of a Sawyer Tower circuit for P-E loop measurements

# 3

# Characterization of oxygen deficient PZT thin films

PZT thin films were deposited on Ti(6nm)/Pt(140nm)/Ti(20nm) coated Si wafers. Detailed process parameters have already been discussed in chapter 2 (experimental part). Coated wafers were processed by rapid thermal annealing (RTA) and conventional annealing (CA) at four different temperatures ranging from $550^0$C, $600^0$C, $650^0$C and $700^0$C.

## 3.1 Results and Discussion

### 3.1.1 Surface morphology

The surface morphology of PZT coated wafers processed by conventional annealing and rapid thermal annealing methods, are shown in Fig.3.1 and Fig.3.2. A crack-free, dense, grainy, and homogeneous surface consisting of roughly spherical particles with a diameter in the range of approximately $50-100$ nm was observed for as$-$deposited PZT specimens. Samples processed by conventional annealing at $650^0$C for 2 h results in a smooth and crack free surface; only relatively few larger particles were observed on the top of the surface or partially embedded in the film (Fig.3.1(b)). For samples processed by conventional annealing at $690^0$C, a few micro cracks with a width of 20nm appeared (Fig.3.1(c)). A temperature increase of up to $720^0$C results in the formation of holes, pits and wider cracks in the film. The surface had a less dense and packed morphology (Fig.3.1(d)). It has been reported that pits and holes formations along the grain boundaries result from lead evaporation [79]. Therefore, we conclude that the crack and hole formation at $720^0$C is due to Pb loss. Fig.3.2(a$-$d) illustrates the microstructure of rapid thermal annealed specimens. Here, the formation of sub$-$micron wide cracks were observed at $550^0$C. Increasing the temperature up to $600^0$C broadens the cracks. However, a significant increase in crack formation and crack size for the films annealed up to $700^0$C has not been observed. Crack formation of rapid thermal annealed PZT specimens has been previously reported, to be caused by the mismatch of the thermal-expansion coefficients of the substrate and the PZT film [80].
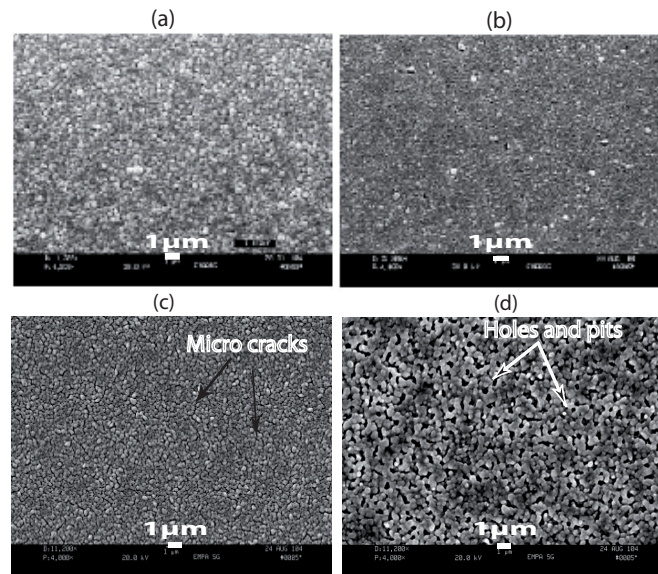
*Fig. 3.1:* Surface morphology of CA processed PZT films: (a) as deposited, (b) $650^0$C, (c) $690^0$C, and (d) $720^0$C
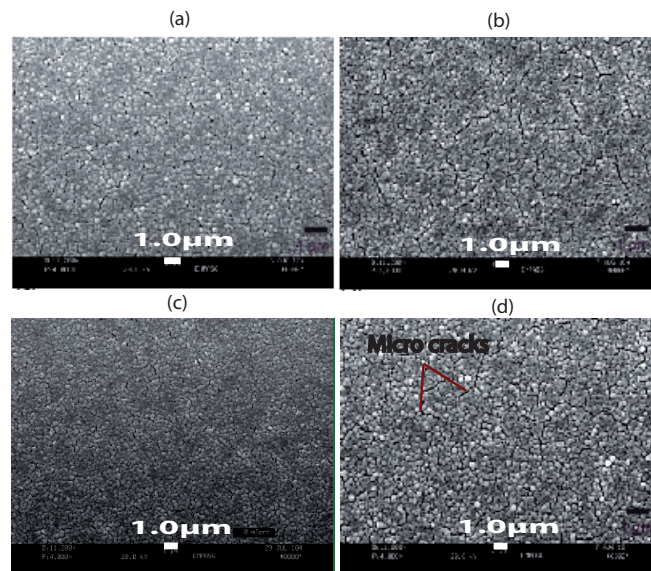


*Fig. 3.2:* Surface morphology of RTA processed PZT films: (a) $550^0$C, (b) $600^0$C, (c) $650^0$C, and (d) $700^0$C
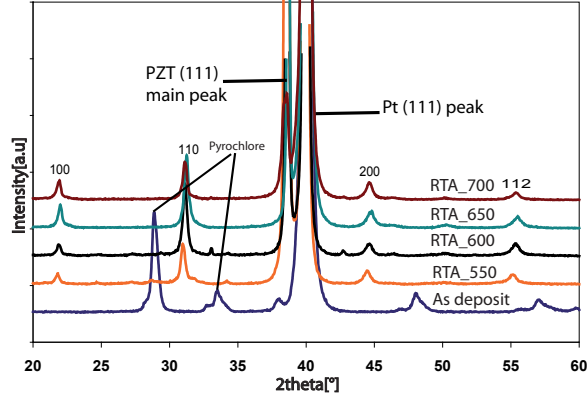
*Fig. 3.3:* XRD patterns of rapid thermal annealing annealed PZT films at $700^0$C, $650^0$C, $600^0$C and $550^0$C

### 3.1.2 Structural investigations

Fig.3.3 shows the XRD patterns of as-deposited and specimens processed by rapid thermal annealing. Pt(111) peak at $40^0$ was observed for all the samples (see Fig.3.3). The comparison of the patterns clearly shows that the annealing procedure had a significant effect on the crystallographic structure. Following the report by Kumar et al. [79] on the intermediate products which are formed during the formation of perovskite PZT, the peaks at $28.9^0$, $33.5^0$, $48^0$ and $57.1^0$ can be attributed to PbO, $PbTi_3O_7$ and $PbZrO_3$. As samples were treated by rapid thermal annealing at temperature from $550^0$ to $700^0$C these compounds react to form ploy−crystalline PZT. The typical (100), (110), (111), and (200) reflections expected for PZT are clearly visible peaks at $21.9^0$, $31.2^0$, $38.7^0$, and $44.8^0$ respectively. The crystal structure formed during rapid thermal annealing is highly dominated by the (111) reflection. This arises from the Pt(111), used as a bottom electrode, which reacts with Pb and formed $Pt_3Pb$(111) as an intermediate metastable product. This enhances the formation of (111) oriented film [81]. No pyrochlore was observed

in rapid thermal annealed samples even at $550^0$C.
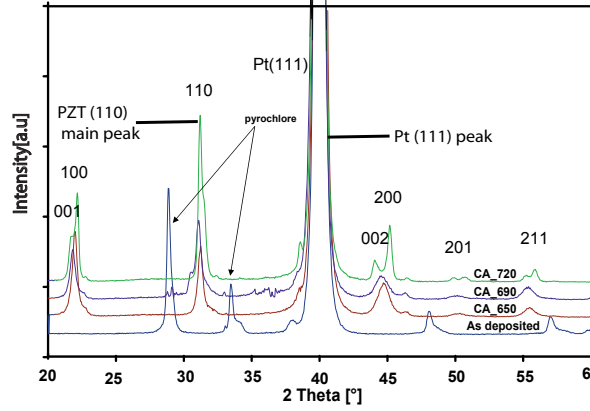


*Fig. 3.4:* XRD patterns of CA annealed PZT films $720^0$C, $690^0$C, $650^0$C, and as deposited

Fig.3.4 shows the X-ray diffraction (XRD) patterns of PZT films processed by conventional annealing at different temperatures. In contrast to the RTA processed samples, CA does not remove the pyrochlore phase completely for lower temperatures between $550^0$C and $600^0$C. At a temperature larger or equal to $650^0$C, PZT pervoskite phase has been appeared. 110 crystallographic oriented reflection dominates the peak intensities for CA-treated specimens. Samples annealed at higher temperature ($720^0$C) showed the peak splitting (Fig.3.4). This peak splitting indicates the existence of tetragonal and rhombohedral phase.

### 3.1.3   Chemical investigation

Chemical analysis of samples treated by rapid thermal annealing and conventional annealing was performed by X-ray photoelectron spectroscopy (XPS). Table 3.1 and 3.2 shows the atomic concentrations and the binding energies (BE)(at.%−extracted from the peak heights) of as-deposited, CA and

rapid thermal annealing-treated PZT films for the Pb4f, Zr3d, Ti2p and O1s signals.

*Tab. 3.1:* Atomic concentrations of PZT

| Sample | Pb At% | Zr At% | Ti At% | O At% | Pb/(Zr+Ti) |
|---|---|---|---|---|---|
| PZT nominal | 20 | 10 | 10 | 60 | 1.0 |
| as deposited | 28 | 8 | 6 | 58 | 2 |
| CA650$^0$C | 22 | 12 | 7 | 59 | 1.2 |
| CA690$^0$C | 25 | 8 | 8 | 59 | 1.6 |
| CA720$^0$C | 28 | 8 | 8 | 56 | 1.8 |
| RTA550$^0$C | 28 | 9 | 5 | 58 | 2 |
| RTA600$^0$C | 26 | 12 | 5 | 57 | 1.5 |
| RTA650$^0$C | 23 | 12 | 7 | 58 | 1.2 |
| RTA700$^0$C | 26 | 11 | 6 | 57 | 1.5 |

*Tab. 3.2:* Binding energies of atoms in PZT thin film

| Sample | Pb BE(eV) | Zr BE(eV) | Ti BE(eV) | O BE(eV) |
|---|---|---|---|---|
| as deposited | 137.9 | 181.4 | 457.6 | 531.2 |
| CA650$^0$C | 137.8 | 181.3 | 457.7 | 530.5 |
| CA690$^0$C | 138.3 | 181.4 | 458 | 529.4 |
| CA720$^0$C | 138.1 | 181.2 | 457.9 | 531.2 |
| RTA550$^0$C | 138.1 | 181.4 | 457.6 | 531.2 |
| RTA600$^0$C | 138.1 | 181.1 | 457.7 | 530.9 |
| RTA650$^0$C | 138 | 181.2 | 457.6 | 529.0 |
| RTA700$^0$C | 138.1 | 181.1 | 457.7 | 531.0 |

Minimal hydrocarbon contamination was detected. The Pb concentration of all the PZT specimens was in the range of $22 - 28$ at%. Note that our XPS data evaluation allows the calculation of atomic percentages with a precision of about $5-10\%$. For RTA treated samples no Pb loss was found

because fast heating rates applied for a short time resulted in small amount of Pb loss. Similar results were obtained by lee and Moulder et.al [82, 83]. The Zr and $O_2$ concentrations of RTA processed samples were found to be close to the values expected from the stchiometry of PZT. However this was not the case with the Ti concentrations of RTA processed samples. This may be caused by the formation of $TiO_x$ near the surface. Little Pb loss was found for the CA processed samples at $650^0$C annealing temperature. At $650^0$C temperature the Pb concentration was 22% and raised to 28% for the annealing temperatue $720^0$C. This surprising result can be explained by Pb aggregation along the grain boundaries of the surface. A lead-rich surface layer may arise from the target containing excess lead (10%) and the aggregation of lead metal due to high temperature anneals to the film surface. Dana et al. suggests that a Pb-rich surface region is an intrinsic phenomenon of the thermal treatment of the deposited material and is not related to a specific film deposition process [84]. The deficiency of oxygen, zirconium, and titanium at surface is considered to be due to the evaporation of Pb-O compounds and the formation of Ti-O and Zr-O compounds [85, 86].

The Pb/(Ti+Zr) ratio has been determined from the XPS of the RTA and CA processed samples and compared to the Pb/(Ti+Zr) ratio of the target that is 1.22. As shown in Table 3.1, the Pb/(Ti+Zr) ratio for RTA and CA processed samples from $550^0$C to $720^0$C, are typically in the range of $1.6 - 2.0$, indicating a Pb-enrichment at the surface. The target ratio of 1.2 is found only for the samples processed by RTA and CA at $650^0$C, indicated that this was the optimal annealing temperature to obtain the complete pervoskite structure. All other samples annealed at different temperatures did not match this ideal ratio.

Fig.3.5(a−d) illustrate the high-resolution spectra of the Pb4f, Zr3d,
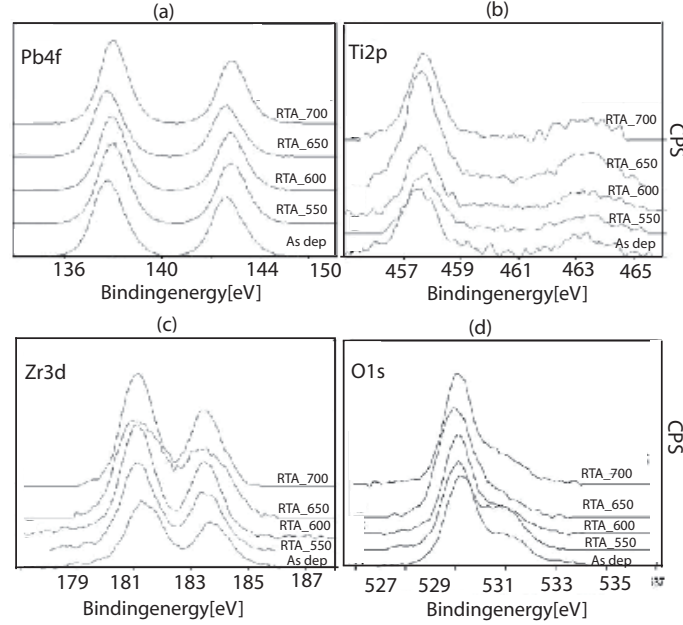
*Fig. 3.5:* Core level spectra of (a) Pb4f, (b) Ti2p, (c) Zr3d, and (d) O1s of as-deposited and rapid thermal annealing-treated samples

Ti2p, and O1s photo emission signals of the as-deposited and RTA treated samples. For all the measurements of the Pb4f, Zr3d and Ti2p signals, the doublet separation matches the corresponding values in the literature [83]. The binding energies of Pb of as deposited and RTA treated PZT specimens is around 138.0 eV for the Pb4f$_{7/2}$ emission and is in good agreement with the published values [87]. Fig.3.5(b) shows the Ti2p signal for as-deposited and RTA treated samples. The BE is 457.6 eV for the Ti2p signals of the as-deposited sample and is constant after rapid thermal annealing within the limit of the BE uncertainty ($\sim 0.2$eV). The BE of the Zr3d$_{5/2}$ signal for all the RTA and CA processed samples are in the range of $(181.1 - 181.4)$ eV. These values differ by at least 1 eV from values for the Zr3d$_{5/2}$ signal of sol gel manufactured PZT samples [85]. This indicated that a full oxidation state

of the Zr species had not been obtained. The O1s signals of as-deposited and rapid thermal annealing-treated samples are shown in Fig.3.5(d). Three different O species were identified in agreement with the literature [86]. As expected, no traces of water were found after rapid thermal annealing treatment, only oxygen derived from the lattice and from hydroxyl species are measured. In contrary, a difference of 0.5 eV in the BEs for the Pb4f signal has been measured for the CA treated specimens at $650^0$ and $690^0$C, indicating an oxidation reaction in the course of the annealing process. A similar effect could not be observed for the rapid thermal annealing samples. RTA has been performed in vacuum at $10^{-5}$ mbar pressure, which prevents oxidation of the samples. The $Ti2p_{3/2}$ binding energy was 457.7 $\pm$0.2 eV for the CA-treated samples. These values are lower in comparison to the measured BE of 458.9 eV for the $Ti2p_{3/2}$ signals in sol gel manufactured PZT samples and indicate a possible coexistence of mixed Pb valence states [85].

## 3.2 Summary

PZT films of thickness around 1.2$\mu$m were fabricated by reactive sputtering from a single metallic target consisting of Pb (55 at%), Zr(22.5 at%), and Ti(22.5 at%) in pulsed DC mode (see chater 1 for pulsed dc method). As a substrate, Si wafer, previously coated by Ti(6nm)/Pt(140nm)/Ti(20nm) tri layers was used. Surface morphologies of as-deposited samples revealed grainy, homogeneous, dense, and crack-free surfaces. CA processing of samples up to 2 h at $690^0$C give rise to low density of cracks. Samples annealed at $720^0$C revealed holes and pits formation, probably due to Pb loss. Rapid thermal annealing of samples at $550^0$C results in relatively low micro-crack formation of multi crystalline PZT specimens. Only a minor increase in crack size and density has been observed at $700^0$C. X-ray diffraction (XRD) con-

firmed the formation of poly−crystalline PZT (perovskite type) at $650^0$C in samples processed by rapid thermal annealing (RTA) and conventioanl annealing (CA). It has been found that RTA and CA processed sample lead to (111) and (110) preferred crystallographic orientation. XPS measurements of all samples revealed typical binding energy (BE) for Pb and O atoms. An incomplete oxidation state of Ti and Zr has been observed. Relatively high Pb/(Zr+Ti) are found for all samples (1.62.0) except for those annealed at $650^0$C (1.2), that matches the Pb/(Zr+Ti) ratio of the target. XPS does not detect the atomic concentration beyond the few nm thickness from the top surface. Hence, a further investigation is essential to understand the distribution of the atoms through the entire film thickness.

# 4

# Compositional analysis and mechanical properties of PZT thin film by GDOES and Nano-indentation

In chapter 3 we described the chemical investigations done on PZT films by X-ray photoelectron spectroscopy (XPS). The major disadvantage of XPS technique is the ability to give compositional analysis only from the near surface region (few nm). Therefore, complete depth profiling has been performed by GDOES (see more detail about GDOES in chapter 2). For the

first time this technique has been used for the PZT thin film depth profiling.

## 4.1 Results and discussion

### 4.1.1 GDOES measurements

Fig.4.1 shows the depth profiles of five samples (as deposited, CA $600^0$C, CA $650^0$C, RTA $600^0$C, and RTA $650^0$C) measured by GD-OES. The measured composition of all samples and the Pb/(Zr+Ti) ratios are summarized in Table 4.1. Note that all these values are obtained by integration over the PZT film thickness. A Pb or Pb-oxide rich (10 nm) zone has been found near the sample surface except for the RTA processed sample at $650^0$C. GDOES does not allow the precise quantitative determination of compositions near the surface region because a stable plasma has not yet been obtained for the accurate analysis. XPS measurements performed on these samples also showed a Pb enrichment near the surface layer. The low Pb concentration near the surface of the samples annealed at $650^0$C can be explained by the evaporation of the lead from the surface. For all samples, we observed an increased Pb concentration at the interface and a corresponding decreased $O_2$ concentration. Such an increase of the Pb concentration at the interfaces (air/PZT and PZT/bottom electrode) of a post-annealed PZT layer has already been reported by Zomorrodian et al. [88]. Similarly, Sun et al. explained the enrichment of Pb at the interface by the high volatility of Pb in between the PZT layer and the bottom electrode that prevents Pb from diffusing into the substrate [89].

The Pb/(Zr+Ti) ratios, except for the sample processed by RTA at $650^0$C were close to the corresponding ratio of the target (see Table 4.1). The oxygen and titanium concentrations are lower and higher than the expected
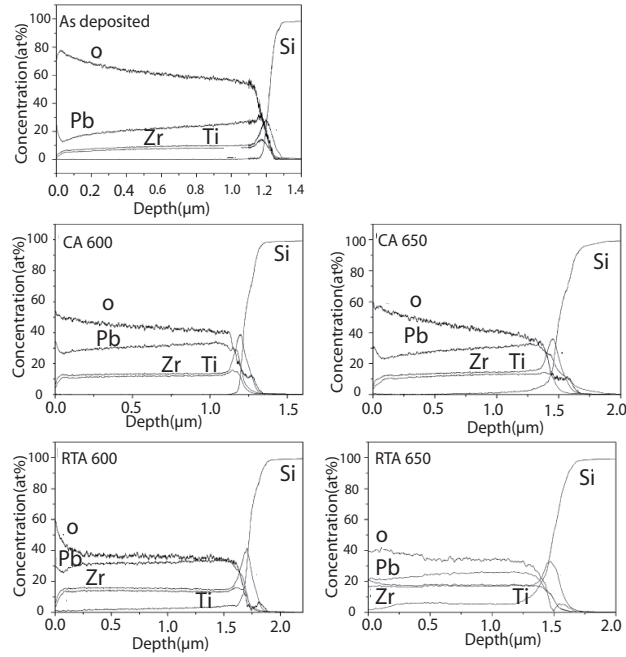
*Fig. 4.1:* GD-OES depth profiles of the different samples. For clarity, only the Pb, Zr, Ti, O and Si signals are shown. (CA: conventional annealing, RTA: rapid thermal annealing)

value, respectively. Furthermore, the Pb/O ratio increases by the thermal treatment. At this stage the cause remains yet unknown. Further experiment presented in chapter 5 will reveal whether these observations are due to sample preparation or caused by instrumental calibration.

### 4.1.2 Nano−indentation measurements

Table 4.2 summarizes the results of the nano−indentation tests presented as average values calculated from several single load−displacement curves. The values in brackets indicate the standard deviation. All annealing methods reduce the hardness and modulus of PZT films compared to the as deposited films. Hardness and Modulus of thermally treated samples are ∼ 2.6 GPa

*Tab. 4.1:* Coating composition and Pb/(Zr+Ti) ratio of the coatings determined by GD-OES

| Name | Pb (at%) | Zr (at%) | Ti (at%) | O (at.%) | Pb/(Zr+Ti) |
|---|---|---|---|---|---|
| PZT nominal | 20.0 | 10.4 | 9.6 | 60.0 | 1.0 |
| As deposited | 21.3 | 7.1 | 8.7 | 62.8 | 1.3 |
| CA $600^0$C | 30.8 | 11.6 | 13.1 | 44.4 | 1.2 |
| CA $650^0$C | 28.6 | 11.8 | 13.6 | 45.2 | 1.1 |
| RTA $600^0$C | 31.7 | 13.5 | 15.3 | 37.3 | 1.1 |
| RTA $650^0$C | 24.2 | 17.0 | 17.9 | 35.8 | 0.7 |

and $\sim$ 67 GPa compared to the $\sim$ 4.1 GPa, $\sim$ 84 GPa hardness and modulus of as-deposited samples. This may due to the softer Pb enrichment in the surface layers, observed by GD-OES and XPS (Fig.4.1). Note that nano$-$indentation performed here only probes about the first 15% ($\approx$180nm) of the coating to avoid influences from the substrate. Our Youngs modulus values is in conformity with the values reported in literature which is around 68 GPa [90, 91, 92, 93]. The hardness of bulk PZT has been reported to be around 9 GPa and for thin coatings even higher upto 17 GPa have been observed [93, 94]. The hardness of thin PZT coatings is expected to depend on the microstructure of the films. For post-deposition annealing temperatures between $600^0$C and 800 $^0$C, Fang et al. found the grain size increases from 62 nm to 78 nm. Hardness of these annealed samples also increases from 6.5 GPa to 16.6 GPa [94]. However, according to Hall$-$Petch theorem hardness generally increases with the decrease in grain size [95]. The Hall-Petch relationship is a relation between the grain size, or crystallite size, and the yield point of a material [96, 97]. This relation says that the larger the grain size of a crystalline material, the weaker it is, that is the smaller its yield strength. The relation is described mathematically by the Hall-Petch

*Tab. 4.2:* Hardness H and Youngs modulus E values obtained from nanoindentation tests

| Name | H($\sigma$H) GPa | E ($\sigma$E GPa |
|---|---|---|
| as deposited | 4.1 (1.0) | 84 (17) |
| CA 550$^0$C | 2.7(0.6) | 73(15) |
| CA 650$^0$C | 2.6(0.8) | 63(12) |
| RTA 600$^0$C | 2.8 (0.5) | 68(15) |
| RTA 650$^0$C | 2.3(0.3) | 63(12) |

equation as follows:

$$\sigma_y = \sigma_0 + \frac{k_y}{\sqrt{d}} \tag{4.1}$$

Where $\sigma_y$ is the yield strength, $\sigma_0$ is the initial yield strength, $k_y$ is a constant and d the mean grain size.

In contrast to the standard Hall−Petch theorem, our hardness values didn't follow this trend. The classic Hall−Petch relationship is based on that grain boundaries act as an obstacle to dislocations. Dislocations require greater amounts of energy to overcome these barriers. Because dislocations are carriers of plastic deformation which increase in material strength. For small grains the deformation mechanism is different. In small grains plastic deformation is not dominated by dislocation motion but by atomic sliding of grain boundaries [94]. In small grains sliding effect dominates because of the larger ratio of grain boundary to the crystal lattice. This mode of deformation leads to observed softening of a material. It has been found in our poly−crystalline PZT thin films that crystallites surrounded by an amorphous material, lead to the lower value of hardness. In addition, the hardness may also be influenced by the Zr/Ti ratio of our samples which was found to be inverse compared to the nominal composition (see Table 4.1). It has been observed that there is a substantial dependence of the fracture

toughness on the Zr/Ti ratio in PZT.

## 4.2   Summary and outlook

PZT coated wafers have been analyzed by GDOES that allowed a fast and quantitative analysis of elemental compositions as a function of depth. Pb/(Zr+Ti) ratio of all annealed samples except RTA at $650^0$C led to a value corresponds to the target value that is 1.0. Pb enrichment is detected at the film−substrate interface. The observed oxygen deficiency arises from an incomplete crystallization of PZT layer , where crystallites are surrounded with a soft amorphous matrix. This also explained the low hardness values found for all samples (as deposited: H= 4.1 GPa and E = 84 GPa: post annealed: H= 2.6 GPa and E = 67 GPa). From the compositional analysis, it has been found that oxygen concentrations are not in the stichometric ratio. In order to obtain the complete perovskite structure, all the atomic concentration has to be matched with the ideal values. In chapter 5 chemical composition and mechanical properties of oxygen rich PZT thin films will be discussed.

# 5

# Characterization of oxygen enriched PZT thin films

In chapter 3 and 4 the chemical composition, the structural and mechanical properties of PZT film deposited by reactive sputtering in $Ar/O_2$ atmosphere were described. The oxygen concentration was found to be significantly lower than needed for the optimum PZT composition. As found in chapter 4 that the low oxygen concentration has been reflected by the poor mechanical properties of the thin films. In order to obtain an increased oxygen content in the films, additional samples have been prepared with a higher partial

pressure of oxygen during the sputtering process under the same annealing procedures.

## 5.1   Structural investigation: XRD

Fig.5.1 shows the XRD patterns of PZT films deposited on Ti/Pt/Ti coated Si wafers prepared at different annealing temperatures.
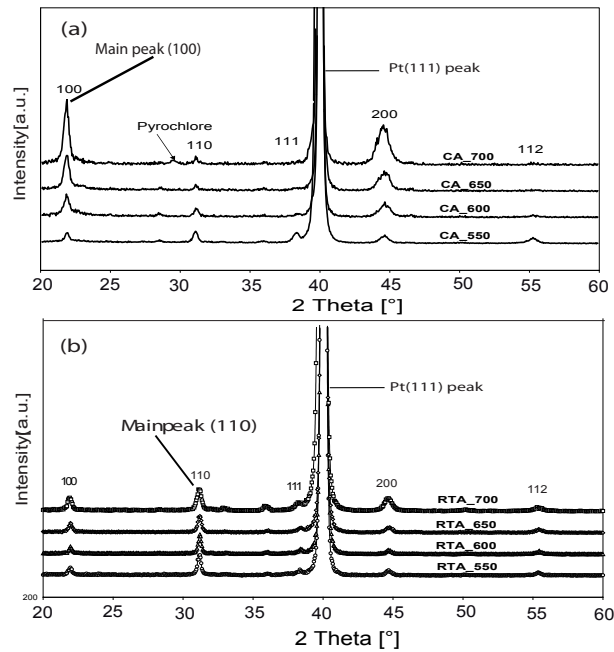


*Fig. 5.1:*   XRD patterns of PZT coated wafers (a) CA processed films, (b) RTA processed films at $700^0$C, $650^0$C, $600^0$C and $550^0$C

In order to compare the structure and composition of the PZT films processed by CA and RTA at different annealing temperatures, all XRD spectra have been normalized with respect to the Pt(111) peak. The PZT structure is identified with by the reflections at $21.90^0$ (100), $31.120^0$ (110), $38.30^0$ (111), $44.90^0$ (200) and $55.40^0$ (211).
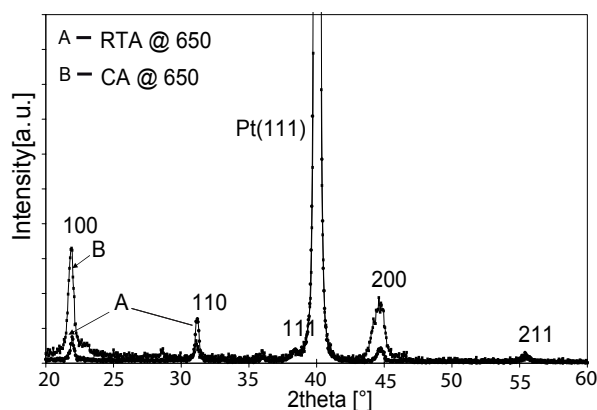
*Fig. 5.2:* XRD pattern of PZT coated wafer (A) RTA at $650^0$C and (B) CA at $650^0$C

CA processed films show a growing intensity of the (100) and (200) peaks and decreasing (110) and (111) peak intensities, when the temperature is raised from 550 to $700^0$C. Hence an improved (100) orientation is found at a higher processing temperature. However at $700^0$C a peak at $29.8^0$ indicating the formation of pyrochlore as a second phase develops. While no such phase appears at $650^0$C. So we conclude a good (100) oriented PZT film is obtained by CA procedure at this temperature.

RTA processed films show a (110) peak that slightly grows with increasing process temperature. The (100) peak also gradually grows with the process temperature but remains considerably smaller than the (110) peak. Hence RTA processed films are predominantly (110) oriented.

The (100) crystallographic orientation of CA and (110) preferred orientation of RTA processed films are clearly visible in Fig.5.2. The difference in orientation can be explained by the influence of the substrate, which affects the nucleation of the PZT species and crystallinity of the oxide phases. This effect is due to the difference in the surface energy of the substrate

and film, which influences the binding energy, surface mobility and critical nuclei size of the atoms [79]. Generally, there are two kinds of nucleation mechanism: hetro−nucleation and homo−nucleation [98, 99, 100]. Usually, hetro-nucleation occurs at the substrate/film interface, which can easily lead to preferential orientation growth resulting from the lattice match. The homo nucleation occurs at internal defects such as impurities in the films, which would lead to a random crystallographic orientation or a dominant growth along the crystal plane with minimum free energy. Also, long heating times lead to aggregation of Pb and formation of PbO(100) on the film surface and the film substrate interface. This PbO(100)/PZT interface might lead to (100) orientation. Thermodynamically, 100 planes are favorable as they take minimum surface energy to form compared to the (110) or (111) orientation [56]. Hence it can be concluded that homo nucleation takes place in the RTA processed film, while hetro nucleation occurs in the CA processed films.

Table 5.1 summarizes the crystallographic orientation of the PZT films with high and low oxygen concentration processed by CA and RTA, respectively. The XRD results show the oxygen deficient films have different crystallographic orientation than the oxygen enriched films for both the annealing processes.

*Tab. 5.1:* Effect of annealing and oxygen concentration on the crystallographic orientation of PZT thin films

| Annealing method | Oxygen deficient | Oxygen rich |
| --- | --- | --- |
| CA | (110) | (100) |
| RTA | (111) | (110) |
| Described in | chapter 3 | chapter 5 |

## 5.2   Topographical investigations: AFM

Micro structure directly influences mechanical and electrical properties of the PZT thin films [101]. Remiens et.al. and Rastogi et.al showed that the grain size of thin films are strongly dependent on the growth processes during film preparation [102, 103].
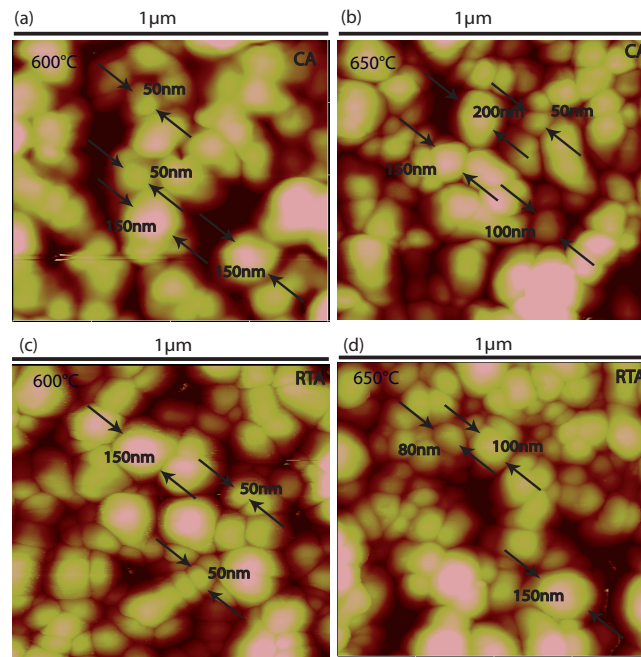


*Fig. 5.3:* Surface topography of PZT thin films : CA processed at (a) $600^0$C, (b) $650^0$C, RTA processed at (c) $600^0$C, (d) $650^0$C

Fig.5.3(a,b) and (c,d) represents the AFM images of CA and RTA processed samples. CA processed film consists of spherical grains with diameters in the range of 100 to 200 nm, while RTA processed films have grains with 50 to 150 nm diameters. The mean grain size is bigger in CA processed films compared to the RTA processed films. The annealing time is much higher in CA treatment, which accommodate enough time for the grains to grow, while

the RTA process is very fast, which suppresses the grain growth leading to a more porous structure. Similar results were obtained by G. Remiens et.al on PZT thin films processed by RTA [101].

It has been found a strong increase of grain size with the process temperature (Fig.5.4). In fact the grain size of a film processed by RTA at $650^0$C is about the double than that of $550^0$C processed films.
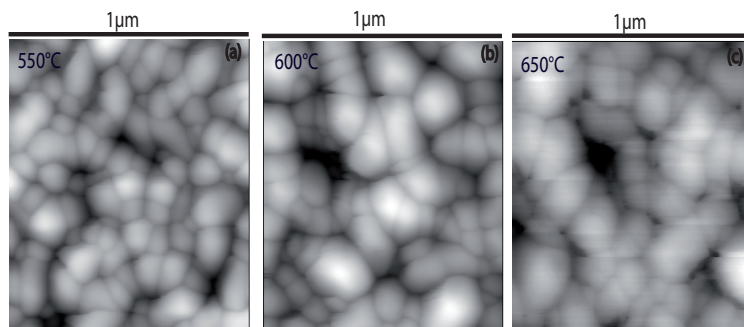


*Fig. 5.4:* Grain size behavior with the increase of annealing temperature of RTA processed PZT films at (a) $550^0$C, (b) $600^0$C, and (c) $650^0$C

Fig.5.5 shows the roughness of all the samples processed by CA and RTA at different temperatures. The measured roughness increases by about $6-10\%$, if the process temperature is raised from $550^0$C to $700^0$C for both annealing samples. This may arise from the finite tip radius, that prevents the tip entering between smaller grains of the films.

## 5.3 Chemical investigation: XPS

XPS was used to measure the atomic concentration in oxygen rich films. Details of the elemental analysis are given in Table 5.2 with an uncertainty of about 5%
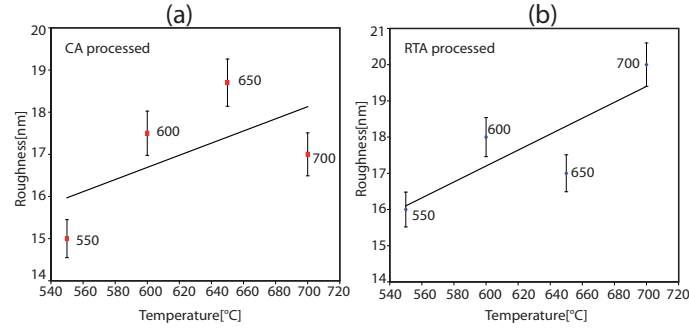
Fig. 5.5: Average roughness of PZT thin films (a) CA processed, (b) RTA processed at different temperature

CA and RTA processed samples have a Zr and $O_2$ concentration corresponding to the value expected for PZT. The Ti concentration is however considerably below the expected values for samples processed by CA and RTA. Verardi et.al revealed that this could be the consequence of the Ti ions react with the chemical neighbor $O_2$, forming $TiO_2$ (+4 valance) or $Ti_2O_3$ (+3 valance) or $TiO$ (+2 valance) oxides. These $TiO_x$ segregate on the surface, reducing the Ti concentrations of annealed films, which can be seen in Table 5.2 [104].
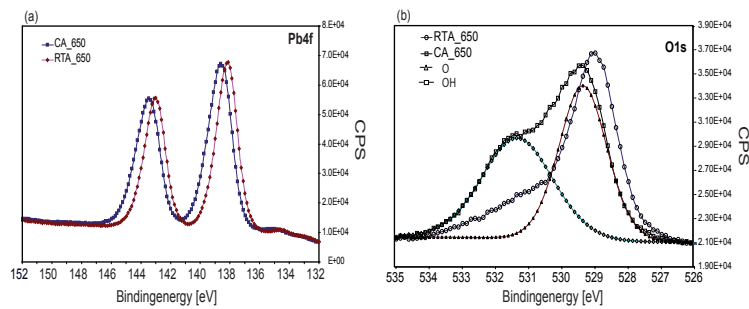


Fig. 5.6: BE for (a) Pb4f and (b) O1s of PZT thin film annealed by CA and RTA at $650^0$C

As the concentration of some elements (Zr and Ti) were very low, high

*Tab. 5.2:* Atomic concentration and Pb/(Zr+Ti) ratio of CA and RTA processed films at different temperature

| Sample name | Pb At% | Zr At% | Ti At% | O At% | (Pb/(Zr+Ti) ratio |
|---|---|---|---|---|---|
| PZT Nominal | 20.0 | 10.4 | 9.6 | 60 | 1.0 |
| PZT Target composition | 22.0 | 10 | 10 | 60 | 1.2 |
| CA $550^0$C | 27.5 | 9.4 | 4.1 | 59 | 2.0 |
| CA $600^0$C | 25.5 | 9.6 | 5 | 60 | 1.7 |
| CA $650^0$C | 23.5 | 9.5 | 4.3 | 63 | 1.7 |
| CA $700^0$C | 23.3 | 10.00 | 5.2 | 62 | 1.5 |
| RTA $550^0$C | 23.5 | 10.2 | 8.8 | 57.7 | 1.2 |
| RTA $600^0$C | 24.5 | 13 | 6.0 | 56.5 | 1.2 |
| RTA $650^0$C | 24.7 | 11.8 | 6.2 | 57 | 1.3 |
| RTA $700^0$C | 22.4 | 11.9 | 5.7 | 60 | 1.2 |
| RTA $650^0$C **(GDOES)** | 21.5 | 8.9 | 9.4 | 59.8 | 1.2 |

resolution XPS was used to improve the signal to noise ratio. Fig.5.6 shows the high resolution XPS spectra of Pb4f and O1s of CA and RTA processed films at $650^0$C. The binding energies are in good agreement with the published data [98, 105]. There is a BE difference of 0.4 eV between the two kinds of heat treated samples, which arises from different oxidation states of Pb [83]. Table 5.3 shows the binding energies (BE) and atomic concentrations (at%) for the Pb4f, Zr3d, Ti2p and O1s signal of CA and RTA processed PZT samples. No difference for the BEs has been found for the Zr3d, Ti2p and O1s with CA and RTA processed films within the uncertainty limit.The Pb/(Zr+Ti) ratio has been determined for all samples and is comparable to the Pb/(Zr+Ti) of the target value, i.e 1.22.

Fig.5.7 shows the Pb/(Zr+Ti) ratio of CA and RTA treated samples. CA processed samples show the higher Pb/(Zr+Ti) ratio than the target ratio, indicating a Pb enrichment at the surface. However, RTA processed samples show a ratio close to our target composition (1.2). A significant increase of the Pb concentration at the interfaces (air/PZT and PZT/bottom electrode)

*Tab. 5.3:* Binding energies (BE) and atomic concentrations (at%) of CA, RTA treated PZT Films

| Sample | Pb 4f(eV) | At% | Zr3d (eV) | At% | Ti2p (eV) | At% | O1s (eV) | At% | Pb/(Zr+Ti) |
|--------|-----------|-----|-----------|-----|-----------|-----|----------|-----|------------|
| PZT Nominal | – | 20.0 | – | 10.4 | – | 9.6 | – | 60 | 1.0 |
| RTA@650$^0$C | 138.0 | 24.6 | 181.3 | 11.8 | 457.8 | 6.1 | 529.3 | 57.4 | 1.3 |
| CA@650$^0$C | 138.4 | 23.4 | 181.5 | 9.5 | 458.0 | 4.2 | 529.6 | 62.8 | 1.7 |

of a post-annealed PZT layer has also been reported by Zomorrodian et al and Sun et al [89, 88]. The enrichment of Pb at the interface is due to the high volatility of Pb between the PZT layer and the bottom electrode, which migrates towards the surface. Pb enrichment was also found near the surface of oxygen deficient PZT films. Since XPS is sensitive to only few nm from the top layer, depth profiling has been performed by GDOES method.
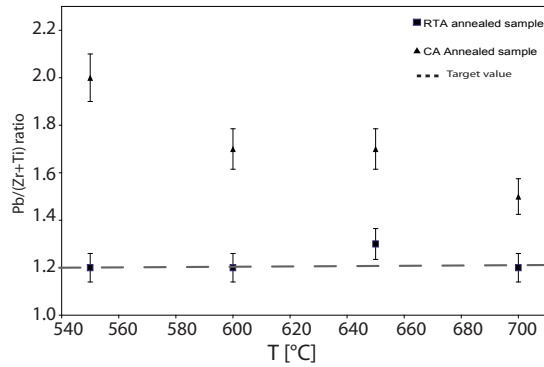


*Fig. 5.7:* Pb/(Zr+Ti) ratio of PZT thin film processed by CA and RTA at 650$^0$C

## 5.4    Depth profiling of PZT thin film by GDOES

Depth profiling of oxygen rich PZT films have been measured by glow discharge optical emission spectroscopy (GDOES). Details about GDOES is already discussed in chapter 2 (section 2.8) Fig.5.8 shows the depth profiling of oxygen rich PZT thin film. Composition of the PZT film is rather homo-
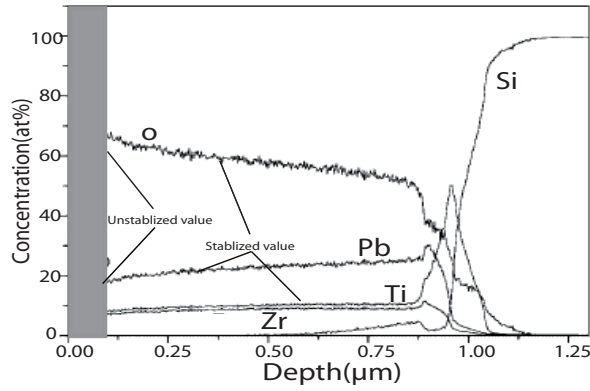
*Fig. 5.8:* Depth profiling of a oxygen rich PZT film by GDOES

*Tab. 5.4:* Coating composition and Pb/Zr+Ti ratio of the PZT coatings deposited using an $O_2$ partial pressure of 0.9 Pa(PZT oxygen deficient) and of 1.8 Pa (PZT oxygen rich) determined by GD-OES.

| Sample | Pb 4f At% | Zr3d At% | Ti$_2$p At% | O1s At% | Pb/(Zr+Ti) |
|---|---|---|---|---|---|
| PZT Nominal | 20.0 | 10.4 | 9.6 | 60 | 1.0 |
| PZT Target composition | 22.0 | 10 | 10 | 60 | 1.2 |
| PZT low oxygen | 31.7 | 13.5 | 15.3 | 37.3 | 1.1 |
| PZT high oxygen | 21.5 | 8.9 | 9.4 | 59.8 | 1.2 |

geneous over the whole thickness with the exception of the near surface zone. The increase of the Pb signal near the coating-substrate interface has also been observed by XPS [78].

Table 5.4 shows the comparison of Pb, Zr, Ti and $O_2$ atomic concentration of oxygen deficient and oxygen rich PZT thin films. For a comparison, the nominal and target composition is also indicated. From these results, it is clear that a high $O_2$ concentration is needed to achieve a composition close to nominal PZT.

*Tab. 5.5:* Young's modulus and Hardness of oxygen rich PZT thin film from Nano
indentation

| Properties | Youngs modulus(E)(GPa) | Hardness(H)(GPa) |
|---|---|---|
| Oxygen rich film | 160 | 10.6 GPa |
| Oxygen deficient film | 63 | 2.3 GPa |

## 5.5  Mechanical properties: Nano-indentation

Mechanical properties of RTA processed PZT thin film at $650^0$C have been
investigated by Nano indentation method. The details of this method has
been described in chapter 2 (see section 2.9). Table 5.5 summarizes the re-
sults of the nanoindentation tests, presented as average values $(15-20$ curves)
calculated from load$-$displacement curves. For comparison, Young's modu-
lus and hardness of oxygen deficient film is also included. It clearly shows
that Young's modulus and hardness increases drastically with the increase
of oxygen concentrations in the films is an indication of an improved crystal-
lization.

## 5.6  Summary

Poly$-$crystalline oxygen rich PZT films have been successfully fabricated
on Si wafers. XRD reveals the (100) and (110) preferred crystallographic
orientation of CA and RTA processed samples. Micro$-$structure of coated
wafers have been measured by AFM. CA processed samples show a dense and
grainy structure, while RTA processed samples reveal the rosette like grain
structure. Grains are bigger in CA processed samples than RTA processed
samples. This is because of grains get enough time to grow in CA methods,
while RTA is fast and suppresses the intermediate grain growth. Grain size

increases when samples are annealed from $550^0$C to $650^0$C. Elemental concentrations are measured by XPS and depth analysis was done by GDOES method. Zr and $O_2$ atomic concentrations are close to the target value. Pb enrichment is found near the surface region of all annealed samples. Young's modulus and hardness has been measured by Nano−indentation method. It is found that oxygen concentration plays an important role to improve the crystallization. Oxygen rich samples show a considerably higher modulus and hardness value compared to the oxygen deficient films. Hence, it can be summarized that PZT thin films have been successfully fabricated and characterized on Si wafers with appropriate atomic concentrations to have high quality films.

# 6

# Electrical properties of PZT thin films

In order to characterize the piezoelectric properties of the various PZT films polarization versus electric field is required. The loops have been measured with the Radiant Technologies (Precision LC, materials analyzer) standard ferroelectric tester, that is based on the Sawer and Tower method [106] (see chapter 2, section 2.10).

Fig.6.1 (a) presents three $P(E)-$loops of PZT films processed by CA at T = $600^0$C, $650^0$C and $700^0$C. The PZT films processed at $600^0$C shows the highest polarization and remanance respectively. ($P_s$ = 55 $\mu$C/cm$^2$, $P_r$ = 37.54 $\mu$C/cm$^2$, $P_r$ = 0.68·$P_s$). The $650^0$C film shows almost the same
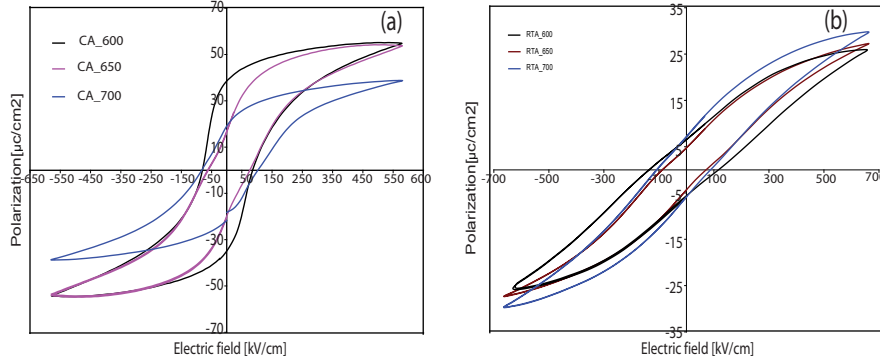
*Fig. 6.1:* PE loop of PZT film processed by CA at $600^0$C, $650^0$C and $700^0$C

saturation polarization ($P_s = 52$ $\mu$C/cm$^2$) but considerably lower remanent polarization ($P_r = 18.42$ $\mu$C/cm$^2 = 0.35 \cdot P_s$) than the film processed at $600^0$C. XRD data of the $600^0$C and $650^0$C processed films show that both are polycrystalline with excellent (100) crystallographic orientation and no second phases exist. XPS data revealed that all the atomic concentrations are close to the stoichiometric value. The lower remanence of the films processed at $650^0$C indicate higher domain wall mobility (less pinning), which is presumably due to larger crystallize size (see chap. 5, section 5.2) and lower defect density obtained at higher process temperature. This is confirmed by the areas (hysteresis energy loss per cm$^3$) enclosed in the $650^0$C loop (A= 21.196 charge/cm$^3$), that is considerably smaller than that of the $600^0$C loop (A = 28.982 charge/cm$^3$).

PZT films processed at $700^0$C shows a much smaller saturation ($P_s = 35$ $\mu$C/cm$^2$) but a comparatively high remanence ($P_r = 20.17$ $\mu$C/cm$^2 = 0.57 \cdot P_s$). XRD shows the presence of pyrochloric phase in addition to the PZT phase, that lowers the saturation polarization and hinders the domain wall motion. The later explains the comparatively higher remanence. XPS data indicate a loss of lead, which may again decrease the saturation po-

larization. Another important feature of $700^0$C loop is that slope of the decreasing field branch does not vanish even in the highest field applied, i.e. the maximum applied field of 550kV/cm is not sufficient to saturate this sample.

The RTA processed samples lead to the strikingly different, so called pinched hysteresis loops (Fig.6.1(b)). The characteristics of these are a low remanence and saturation is not obtained for the same maximum field applied. In contrast to the CA processed films, here the maximum polarization is obtained for the films processed at the highest temperature ($700^0$C). The areas enclosed in the loops ($A_1 = 12.030$ charge/cm$^3$, $A_2 = 7.941$ charge/cm$^3$, $A_3 = 6.409$ charge/cm$^3$ for T = $600^0$C , T= $650^0$C , T = $700^0$C ) are considerably smaller than those of the CA processed samples ($A_1 = 28.982$ charge/cm$^3$, $A_2 = 21.196$ charge/cm$^3$, $A_3 = 22.534$ charge/cm$^3$ for T = $600^0$C, T = $650^0$C, T = $700^0$C). This indicates a typical hard axis behavior of the polarization as a function of applied electric field. XRD data shows the all RTA films are (110) oriented, whereas CA films are (100) oriented. For composition close to the morphotoric phase boundary (MPB), the spontaneous PZT polarization vector is along the [100] and [111] direction but not along [110] axis [14]. For the (110) oriented films the electric field will thus not follow one of the spontaneous polarization directions (easy axis). Hence the hysteresis process will be governed by polarization rotation away from the easy axis and thus show a typical hard axis behavior. Saturation polarization will thus never be reached.

Fig.6.2 shows various minor loops for the $700^0$C CA sample for different maximum applied fields. For a major loop one would expect that no hysteresis occurs at a very high fields (decreasing branch falls onto increasing branch beyond a sufficiently high field). Also one would expect that the polarization
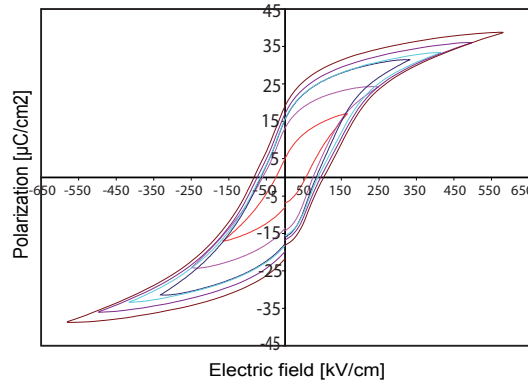
*Fig. 6.2:* Polarization vs electric field loop of CA processed samples at 700

reaches a well defined maximum value,i.e. the saturation polarization (see Fig.6.3 (b)). Obviously saturation in the classical sense is not obtained for most of the loops in Fig.6.1 (a) and Fig.6.1 (b). An almost horizontal tangent can be fitted to the CA processed loops at $600^0$C and $650^0$C indicating that saturation may have been obtained for these films. Note that in contrast to the ferromagnetic material a horizontal tangent will never be completely obtained for a ferroelectric material because individual $TiO_6$ polarizable units can continue to be distorted with increasing the polarization (see chapter 1, section 1.4) [12]. In this case the saturation polarization is obtained by extrapolation of the high field tangent to E = 0 gives saturation polarization. Nevertheless the decreasing and increasing branch of hysteresis loop must fall together, otherwise loop is a minor loop(see Fig.6.3 (b) in contrast to Fig.6.3 (a)).

In ferroelectric material a true major loop may never be obtained because electric breakdown occurs before saturation is reached. To overcome this problem a new procedure to estimate the saturation field and polarization from a series of minor loops has been developed.
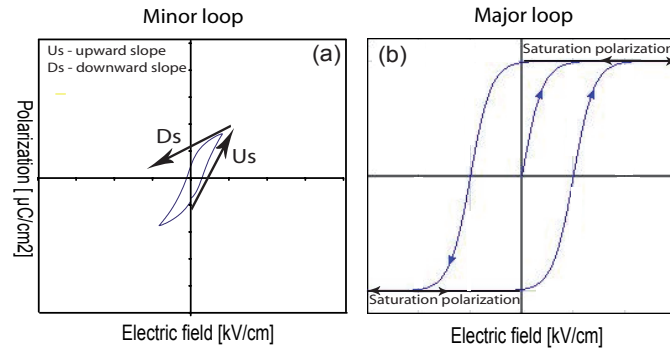
*Fig. 6.3:* Minor and Major loop in hysteresis

In this method, in a first step, a tangent is fitted to the upward and downward branch of the maximum applied field to all the minor hysteresis loops to acquired for a specific film. With increasing maximum field the shape of the minor loops will evolve into the typical shape of a major loop, that shows equal slopes for the upward and downward branches (compare Fig.6.3 (a) to Fig.6.3 (b) and imagine how the minor loop evolve into the major loop for increasing maximum field).

In a second step the values of upward slope and downward slope are plotted as a function of the maximum applied electric fields (Fig.6.4 (a,b,c) for CA films and Fig.6.5 (a,b,c) for RTA films processed at $600^0$C, $650^0$C, and $700^0$C, respectively). Surprisingly, straight line can be fitted to the collections of upward slope and downward slope, that can be extrapolated beyond the maximum applied electric field.

The electric field for two slopes intersects to each other i.e. the upward and downward slope become equal, the saturation polarization is obtained for a sample, which is ferroelectric and has a negligible polarizibility. The point of intersections where saturation is achieved indicates a vanishing slope. For a material that contains a phase with a high polarizibility, one would expect an intersection point with a finite positive slope, i.e. the material contain
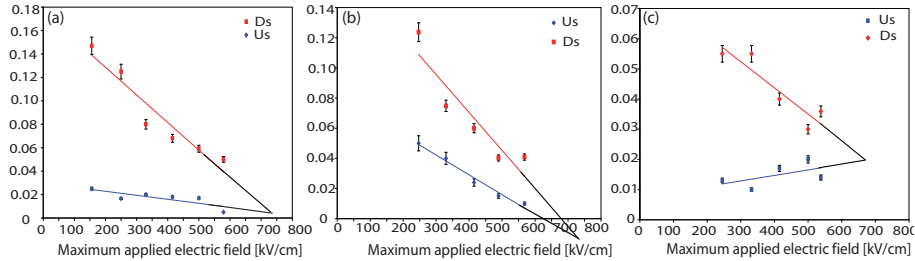
*Fig. 6.4:* Upward ($U_s$) and downward slope ($D_s$) of CA processed films at (a) $600^0$C, (b) $650^0$C, (c) $700^0$C

polarization even if saturation is obtained.

For the CA processed films at $600^0$C and $650^0$C, the intersection point indeed shows an almost vanishing slope, so there is little polarizibility beyond the saturation polarization. Saturation would have been reached around 750kV/cm, which is slightly higher than the maximum field that we could apply with our equipment. This confirms that these films indeed have an excellent ferroelectric properties and do not contain a polarizable phase, and that the polarization axis is parallel to the applied field. This nicely confirms the XRD data that showed a 100 orientation and absence of any pyrochlore (highly polarizable) phase. The CA processed films at $700^0$C is surprisingly different. Here the intersection points clearly shows a finite slope. This is a strong indication that a horizontal tangent could have been obtained, if saturation polarization would have been reached at electric field higher that the ones we could apply with our equipment. Hence, the material remains highly polarizable well beyond saturation. This can be explained by the presence of the pyrochloric phase obtained by XRD (see chap. 5, Fig.5.1).

The analysis of RTA films (Fig.6.5 (a,b,c)) again shows that the films
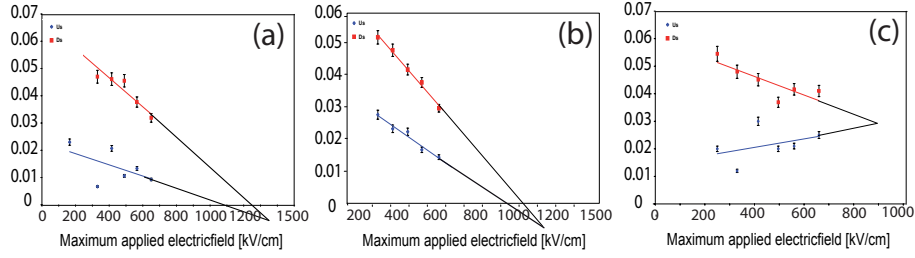
*Fig. 6.5:* Upward ($U_s$) and downward slope ($D_s$) of RTA processed films at (a) $600^0$C, (b) $650^0$C, (c) $700^0$C

processed at $600^0$C and $650^0$C respectively, can be saturated and have a vanishing polarizibility. However, the field required for saturation is around 1250 kV/cm, which is much higher that the 700 kV/cm needed for the CA processed films. This is explained by a hard axis behavior. The RTA films have a 110 orientation such that the electric field is not parallel to the saturated polarization axis of the PZT structure (see XRD data, Fig.5.1). Again the films processed at $700^0$C shows a non vanishing slope after saturation is reached; hence showing the presence of the highly polarisible pyrochloric phase.

## 6.1   Summary

P(E) loops of CA and RTA processed samples at $600^0$C, $650^0$C and $700^0$C have been measured. CA processed samples at $600^0$C and $650^0$C show higher value of saturation polarization compare to that at $700^0$C annealed films. Loss of polarization at higher annealing temperature indicates the presence of pyrochlore phase which has been confirmed by XRD pattern (see chapter 5, section 5.1). This secondary phase lowers the saturation polarization and hinders the domain wall motion. The RTA processed samples lead to the pinched hysteresis loops. These samples have a low remanance and saturation

polarization is not obtained for the maximum applied field. These pinched hysteresis are due to the presence of different domain walls in [100] direction, which makes them difficult to polarize along the applied field, as polarization vector is along [111] and [100] axis. A new method has been developed to estimate the saturation polarization of thin films from minor loops and to detect the presence of the highly polarizable pyrochloric phase.

# 7

# Development and application of lead zirconate titanate (PZT) coating on fibers

## 7.1  Introduction

In recent years considerable efforts have been focused on the development of intelligent materials and structures. These materials have an ability to adapt to their environments through a controlled modification of their mate-

rial properties [107, 108]. Intelligent material systems have an advantage over conventional ones as sensing and response functions are built into them using a chemical or morphological structure [109]. PZT has excellent piezo−electric properties and is therefore widely used for the sensor and actuator applications. PZT can be used to measure the changes in pressure and strain in a material by generating an electrical response. These electrical signals can be used to control actuators, to trigger alarms or to switch systems on or off.

In most applications solid blades of PZT in various geometrical shape in the form of PZT films deposited onto flat substrate are used. Here, we concentrate on the fabrication of fiber having PZT structure. Such electro active fibers can be fabricated by the viscous suspension spinning process (VSSP) [52], by extrusion of polymer / PZT blends or by sol−gel processes [53]. The disadvantage of these fabrication method is the low stability of fiber under mechanical stress and the brittleness [110].
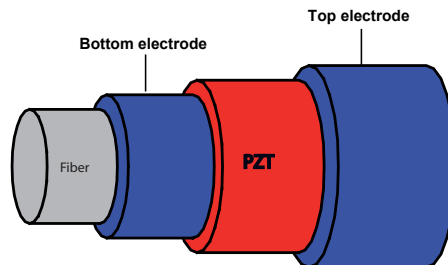


*Fig. 7.1:* Hybrid fiber setup

In order to overcome these mechanical deficiencies, hybrid fibers consisting of a core fiber with good mechanical properties, a bottom electrode, a PZT coating and a top electrode were fabricated (Fig.7.1) [111, 112]. For the core fiber different materials were used. These were glass fiber with a Ti/Pt/Ti or Au layer as a bottom electrode, steel and Cu fibers. In

case of the later two materials the conducting fiber itself served as the bottom electrode. The Ti(6nm)/Pt(140nm)/Ti(20nm) on glass fibers was originally chosen to have a substrate that is as similar as possible to the Ti(6nm)/Pt(140nm)/Ti(20nm) Si wafer substrate. However, the only 126 nm thick Ti/Pt/Ti trilayer on the glass fiber did not enhance the mechanical properties of the brittle glass fiber sufficiently to allow its successive use as a sensor. For this reason, we decided to use a commercially available Au coated glass fiber with a Au thickness of about 10 $\mu$m. This fiber is extremely rugged and so easy to handle. The steel and Cu fibers were used as an alternative to the glass core fiber.

## 7.2 Cleaning of fiber

Before PZT deposition on fibers, cleaning was an essential part to get rid of unwanted adsorbate from the surface. A better adhesion of the coating can thus be obtained. Standard mono mode optical glass fibers with a 125 $\mu$m cladding diameter and 9 $\mu$m core have been used as a substrate. First, the polymer jacket and sizing is removed by using insulation stripper tongs from the glass fibers. Furthermore, fibers are cleaned ultrasonically in dichloromethane and 2-iso propanol solvents for 10 min. The cleaned fibers, approximately 10 cm long are then placed in a specially designed fiber holder within the plasma reactor for PZT coatings (see Fig.7.2 (c)). Steel, Cu and Pt metal fibers were also cleaned ultrasonically in alcohol ($C_2H_5OH$), diluted nitric acid (1:10 ratio) and acetone for 10 min each.
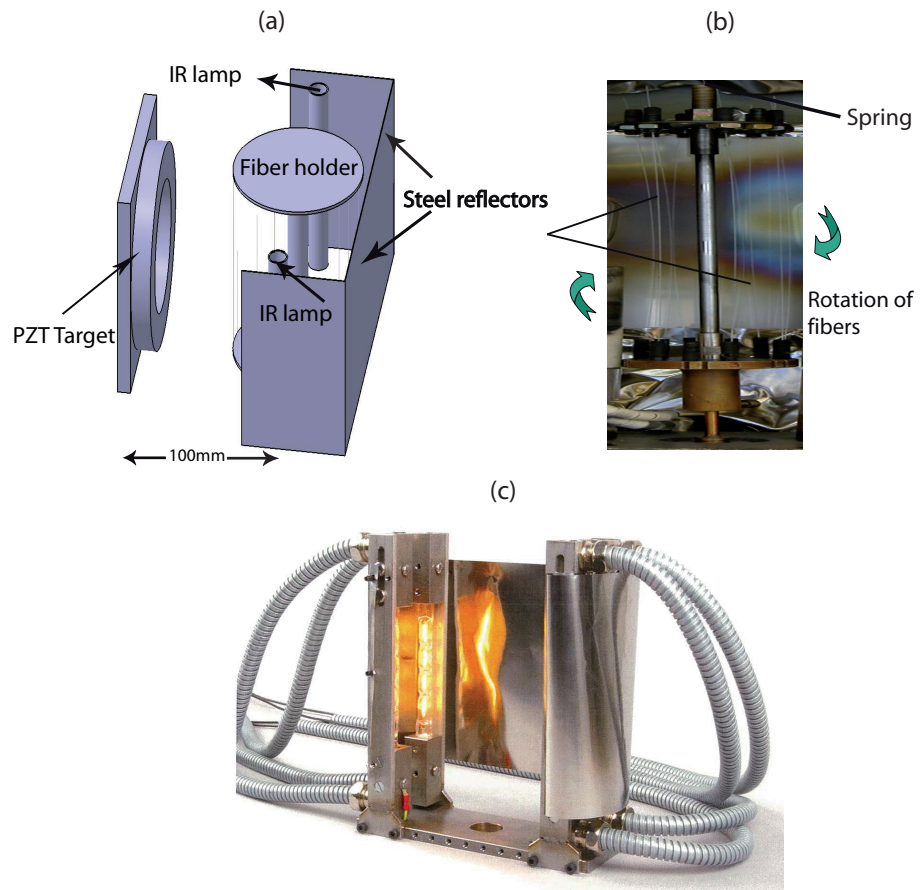
Fig. 7.2: (a) Schematic diagram of PZT deposition on fibers, (b) Novel fiber holder for the deposition on fibers (c) RTA setup for PZT coated fibers

## 7.3 Experimental setup

Fig.7.2 (a) shows an experimental setup for the PZT deposition on fibers. A 10 inch diameter PZT target is placed about 10 cm away from a fiber carrier (Fig.7.2 (b) that is rotating with 10 rpm inside an infrared oven (Fig.7.2 (c). This oven was heated to a temperature of $250^0$C during the PZT deposition. Then RTA with temperature upto $700^0$C was used for further proceeding to obtain the correct PZT structure and chemical composition. In contrast to the PZT deposition on Si wafers here, only RTA was used. CA method was not successful because the vacuum conditions substantially deteriorated when the large oven was heated at such high temperature.

## 7.4 Process procedure

The process parameters for the PZT deposition on fibers were adapted from those used for the PZT deposition on flat substrate. Various test depositions were done at different substrate temperature on these fibers (measured by the thermocouple inside the oven, Fig.7.2 (c)) and different oxygen partial pressure with the correct stoichiometry (measured by XPS) was obtained. Table 7.3 summarize the optimum process parameter and compare them to those used for the PZT deposition on the Si wafers. The optimum deposition parameters and oxygen flow of the fiber and the flat substrate are surprisingly different.

Here, we can only speculate about the reasons. In case of deposition on fibers the temperature is measured with a thermocouple that is loosely hanging into the oven. The mechanical anchoring of the thermocouple is done outside the oven. There may thus be some heat transport from the end of the thermocouple to this mechanical support. As a consequence the

measured temperature may be lower than the actual temperature inside the oven. This may explain in part the reason behind the large difference. Surprisingly, a much higher oxygen partial pressure was needed to obtain a good stoichiometric on the wafer substrate. In case of rotating fiber substrate oxidation may progress better on the part of the fiber surface that is rotating away from the sputter source (see Table 7.3).

*Tab. 7.1:* PZT deposition on different fibers

| Process parameter | Fiber | Wafer |
|---|---|---|
| Power on the target | 250 W | 250 W |
| Base pressure | $10^{-7}$ mbar | $10^{-7}$ mbar |
| Deposition pressure | 0.020mbar | 0.020mbar |
| Target to substrate distance | 100 mm | 100 mm |
| Substrate | Ti(20nm)/Pt(140nm)/Ti(6nm), Au, steel, Cu | Ti(20nm)/Pt(140nm)/Ti(6nm) |
| Deposition time | $9 - 10$ hrs | $9 - 10$ hrs |
| Substrate temperature | $250^0$C | $490^0$C |
| Gas flow | Ar (50 sccm), $O_2$ (30 sccm) | Ar (60 sccm), $O_2$ (90 sccm) |
| Rotational speed | 10 rpm | $-$ |
| Thickness | $1\mu$m | $1\mu$m |

In order to perform electrical measurements a Au top electrode was deposited using the deposition parameter shown in Table 7.4

*Tab. 7.2:* Au deposition for top electrode

| Bp | Wp | Power (W) | Ar (sccm) | time(min) | thickness (nm) |
|---|---|---|---|---|---|
| 5.0 * $10^{-7}$ | 20 | 250 | 60 | 6 | 300 |

- Bp : Base pressure (mbar)

- Wp : Working pressure ($\mu$bar)

## 7.5  Results and discussion

### 7.5.1  Surface Morphology: SEM

SEM has been used to image the morphology of the PZT coated fibers, deposited on the Au coated glass fiber, the steel and the Cu fiber.
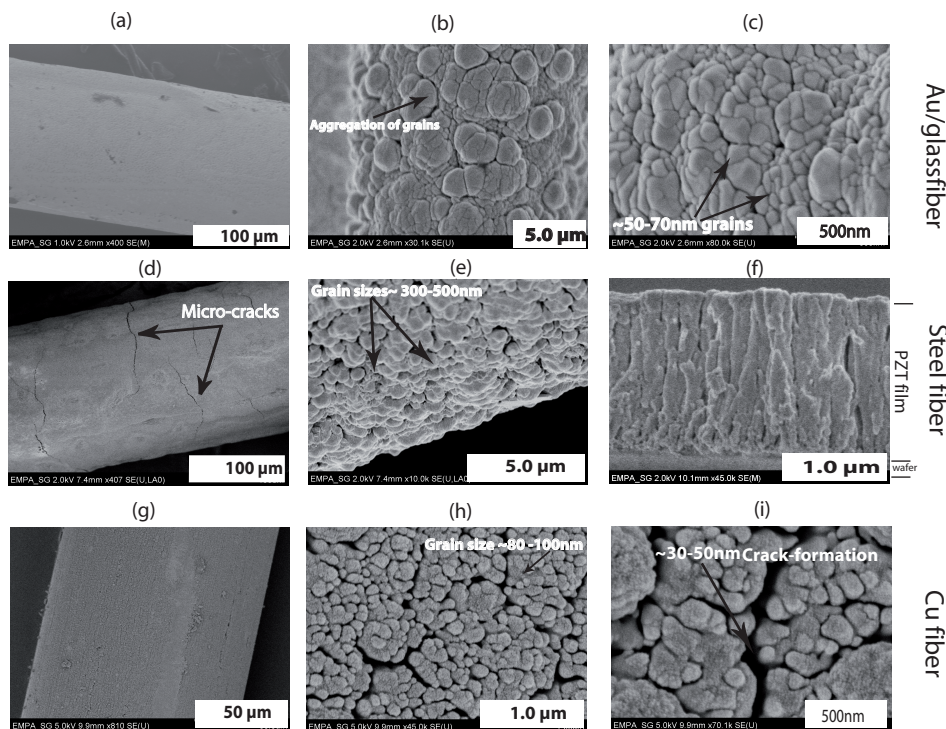


*Fig. 7.3:* SEM images of PZT coated (a) Au coated glass fiber, (b) Steel fiber, (c) Cu fiber

On the Au coated glass fiber Fig.7.3 (a, b, c) a dense and crack free film morphology was obtained. The grain size of 50−70 nm were formed very similar to that obtained on the wafer substrate. On the steel fiber (Fig.7.3 (d)) micro−cracks were formed. The grain size is in the range of 200−500nm and thus considerably larger than that of the grains on the Au fiber (Fig.7.3 e, f). The appearance of micro−cracks may be due to the larger differential

thermal expansion coefficient of PZT versus steel compared to PZT versus Au on glass. The difference in grain size may arise from different surface energies. The PZT coating on Cu fiber shows the worse and wider cracks (Fig.7.3 (g, h, i)). This confirms our explanation that the crack formations are due to the difference in thermal expansion coefficient of PZT and the substrate. The grain sizes on the Cu fiber are between 60−80 nm, which are slightly higher than on Au coated glass fibers but still considerably smaller than on steel.

The cross sections of the PZT coating on the steel fibers (Fig.7.3 (f)) shows a nice columnar grain growth towards PZT coating.

If we compare the morphologies of all PZT coated fibers, it can be summarized as follows:

- PZT coatings are well crystallized on all metallic as well as on non metallic fibers.

- Spherical grains and dense micro structure are observed for all fibers.

- No micro cracks are observed on Au coated glassfibers. Some micro−cracks have been observed on the PZT coated Cu and steel fibers.

- Broad distribution of grain sizes have been observed. Grains in coated steel fibers show the biggest grain size($\approx$ 300 nm) among all, which might be due to a lesser number of nucleation centers formed on the steel fiber. This leads to a slower grain growth in the starting phase of the coating process, resulting in bigger grain size on steel substrate. All other coated fibers show grain sizes in the range of 60 to 200 nm,

- Columnar like grain growth has been observed for coated steel fiber.

- PZT grain sizes on wafers are almost similar to the grains on fiber substrate except for the PZT grains on steel fiber. Hence, it can be concluded that grain growth is identical in both plane and cylindrical substrate.

### 7.5.2  Structural investigation: XRD

The pattern of the as-deposited samples show the typical (222), (400), and (440) reflections of the pyrochlore structure $AB_3O_7$ at $29.5^o$, $33.2^o$, and $49.2^o$ . Fibers processed by rapid thermal annealing form a perovskite PZT structure that is identified by the peaks at $31.1^o$ (110), $38.3^o$ (111) and $55.4^o$ (211). All the PZT coated fibers show poly−crystalline behavior with (110) preferred crystallographic orientation. The X-ray diffraction (XRD) patterns of PZT-coated Au/glassfiber, steel and Cu fibers are shown in Fig.7.4 − 7.6.



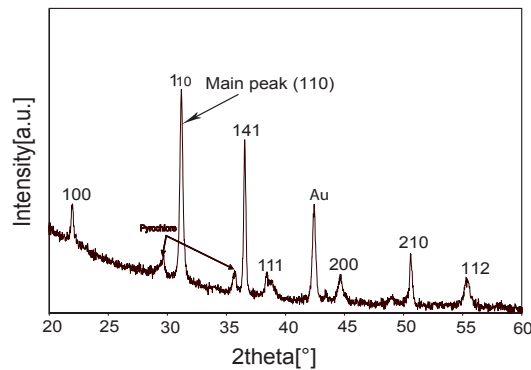*Fig. 7.4:* X−ray diffraction pattern of PZT coated Au/glassfiber, RTA processed @$650^0$C

In order to find out the effect of annealing time on the crystallinity, PZT coated steel fibers have been processed by RTA at $600^0$C and $650^0$C for 2 min each and at $650^0$C for 6 min respectively. The intensity of the (110) peak increases dramatically with the annealing temperature from $600^0$C to $650^0$C
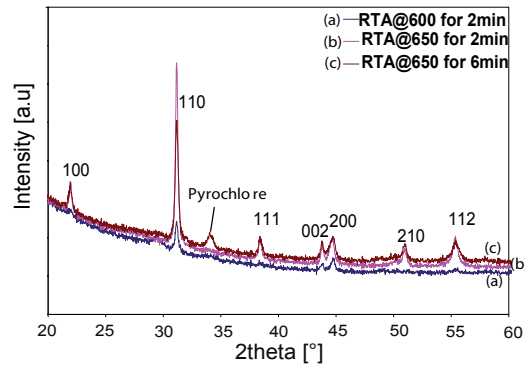
*Fig. 7.5:* X−ray diffraction pattern of PZT coated steel fiber at different annealing temperatures. (110) preferred crystallographic orientation is observed. Pyrochlore as a second phase has been observed for the fibers with long annealing time ($650^0$C for 6 min).

(2min each). PZT coated steel fibers annealed at $650^0$C for 6 min results in a decrease of (110) intensity peak and the appearance of a pyrochlore phase (Fig.7.5). This can be explained by the evaporation of lead that induces a degradation of the PZT structure, leading to a lower crystallinity of the films and the appearance of second phase [113]. If we compare the X-ray diffraction patterns (XRD) of all PZT coated fibers (Fig.7.7), the following conclusions can be deduced:

- Poly−crystalline PZT is obtained on all the fibers.

- Complete perovskite structure is observed without any pyrochlore phase except for RTA processed steel fibers for longer time (6 min).

- All coated fibers show (110) preferred crystallographic orientation.

- RTA processed wafers (oxygen rich, see chapter 5, section 5.1) and fibers show the identical (110) preferred crystallographic orientation.
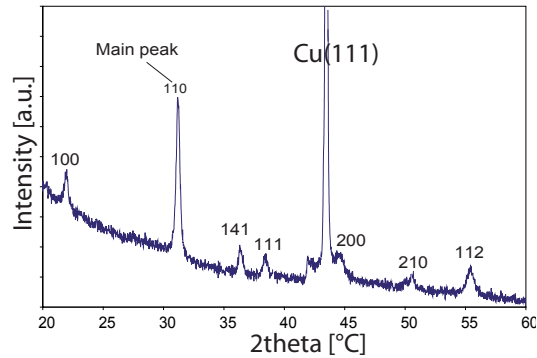
*Fig. 7.6:* X−ray diffraction pattern of PZT coated Cu fiber, RTA processed @650$^0$C
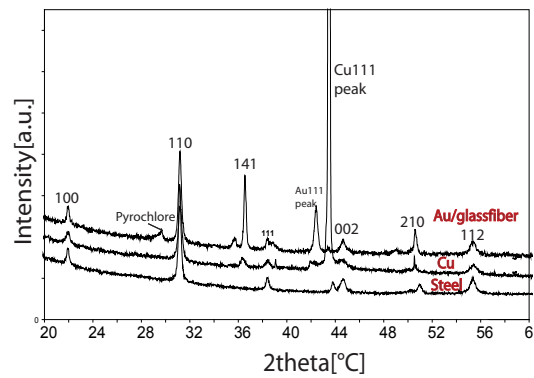


*Fig. 7.7:* X-ray diffraction pattern of PZT coated fibers. (110) preferred crystallographic orientation has been observed on all fibers

- It has been found that 650$^0$C is an adequate annealing temperature for PZT deposition on fiber by using the experimental set up described in this study.

### 7.5.3  Chemical Investigation: XPS

The atomic concentrations and oxidation states of the elements present at the fiber surfaces are measured by XPS analysis with an uncertainty of 5 to 10%. Details of the atomic concentrations are given in Table 7.6. The atomic

concentrations of Pb, Zr, Ti and O atoms are close to the nominal value for PZT. Small amount of lead loss is observed for the RTA processed (for 6 min) PZT coated steel fibers. Due to long annealing time (6 min) Pb evaporates, which results in a reduced Pb concentration in the films. These results are in agreement with the X-ray diffraction results (see Fig.7.5), where a loss of crystallinity is also observed for long annealed (6 min) films. Increased amount of oxygen concentration has been observed for almost all coated fibers. This might be due to the absorption of water ($H_2O$) from atmosphere during the exposure of samples in the air. The Pb/Zr+Ti ratio of the coated fibers are in between 1.0 to 1.4 , which are comparable to our target value of 1.2.

*Tab. 7.3:* Elemental analysis of PZT coated fibers by XPS

| Sample | Pb At% | O At% | Zr At% | Ti At% | Pb/(Zr+Ti) |
|---|---|---|---|---|---|
| PZT nominal | 20 | 60 | 10 | 10 | 1.0 |
| PZT Target | 22 | - | 10 | 10 | 1.2 |
| PZT/Au/coatedglassfiber | 20 | 64 | 8 | 6 | 1.4 |
| PZT/steel/ RTA600$^0$C for 2min | 20 | 66 | 10 | 8 | 1.1 |
| PZT/steel/ RTA650$^0$C for 6min | 18 | 66 | 10 | 8 | 1.0 |
| PZT/Cu | 22 | 60 | 9 | 10 | 1.1 |

All coated fibers are further analyzed by medium resolution XPS measurements to examine the chemical environments of the elements. As the concentration for some elements are very low, medium resolution measurements have been performed to improve the signal to noise ratio.

Table 7.7 shows the binding energies (BE's) of Pb, Zr, Ti and O atoms of PZT coated fibers. Medium resolution spectrum of PZT coated steel fiber is shown in Fig.7.8. From the Pb 4f spectrum, it can be seen that $Pb^{4+}$ and $Pb^{0+}$ is formed, and the corresponding binding energy is 138.8 and 136.2 eV

*Tab. 7.4:* Binding energies (BEs) of Pb, Zr, Ti and O atoms (at%) of PZT coated fibers

| Spin orbit coupling (LS) | Binding energies (eV) | | | |
|---|---|---|---|---|
| Atoms | PZT/ Au/glassfiber | PZT/ steel | PZT/ Cu | PZT/ Pt |
| Pb4f(7/2,5/2) | 135.0, 140.0 | 135.0, 140.0 | 138.0, 143.8 | 138.0, 140.0 |
| Zr3d (5/2,3/2) | 177.5, 180.0 | 178.5 , 181.5 | 181.5, 184.0 | 179.0, 182.0 |
| Ti 2p (3/2, 1/2) | 458.5, 463.0 | 461.0, 465.5 | 459.0, 464.0 | 461.0, 466.0 |
| O1s | 526.0 | 527.0 | 530.0 | 528.0 |

respectively [114]. The signal at a binding energy of 136.2 eV is associated with metallic Pb. The appearance of metallic Pb can be attributed to the reduction of the $Pb^{4+}$ ions to metallic $Pb^{0+}$ [111, 112]. The peak at a binding energy of 138.8 eV corresponds to the formation of lead oxide in the PZT.

The Zr3d spectrum shows the formation of $Zr^{4+}$ and $Zr^{0+}$ ,with binding energies at 179.0 eV and 183.5 eV . These values are in agreement with the reported values [115]. Metallic $Zr^{0+}$ has been found in PZT coated fibers, indicating an incomplete oxidation of Zr atoms.

The O1s signal consisting of broad signals around 530 eV and 531.8eV are in agreement with the values reported for PZT thin films [116, 117, 118, 119]. The O1s signal results from the interaction of oxygen with Pb,Ti and Zr atoms, forming oxides. In PZT film, the softening of bonds is caused by the bonding interaction in Ti−O, Zr−O and Pb−O with binding energy at 531.8 eV. The fitting of O1s signal reveals for all the fibers the presence of OH−groups at the surface. These hydroxyl groups come from the surrounding atmosphere, while exposing the samples to air.

The broad Ti $2p_{1/2}$ signal in the PZT film has been associated with the various charge state of Ti [117]. The higher binding energy (459 eV) of Ti $2p_{3/2}$ corresponds to $Ti^{4+}$. Binding energies at 456 eV correspond to a

chemically reduced state in the form of $Ti^{3+}$ or $Ti^{2+}$. So, the Ti in PZT coated fibers exist in a mixed valance state like $Ti^{4+}$, $Ti^{3+}$, $Ti^{2+}$.
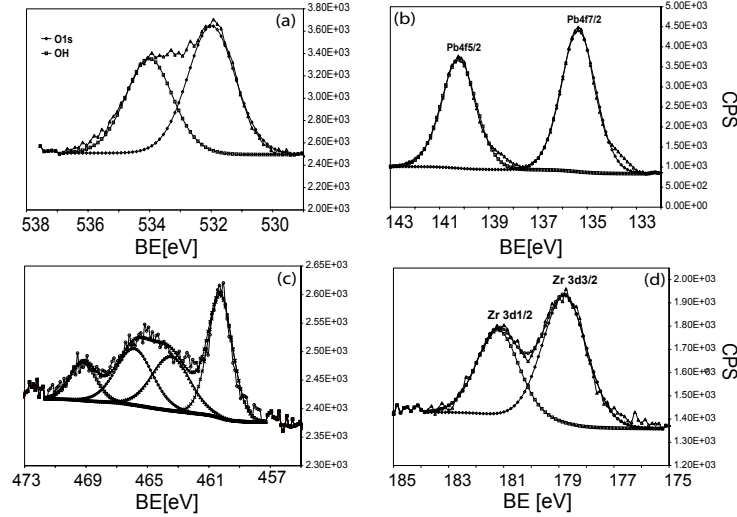


*Fig. 7.8:* Medium resolution spectrum of PZT coated steel fiber at $650^0C$: (a) O1s, (b) Pb4f, (c) Ti2p and (d) Zr3d signal

## 7.6 Application of PZT coated fibers

Piezoelectric coated fiber based devices can be used in many applications such as energy harvesting, sensors, actuators, optical phase modulator, structural health monitoring etc. In the next section the use of PZT coated steel fibers for sensor application is demonstrated. Thereby, the device transforms the received information from the operating environment (vibrations or mechanical deformations) into electrical signals due to the electrical mechanical coupling behavior (see chapter 1, section 1.1) of PZT.
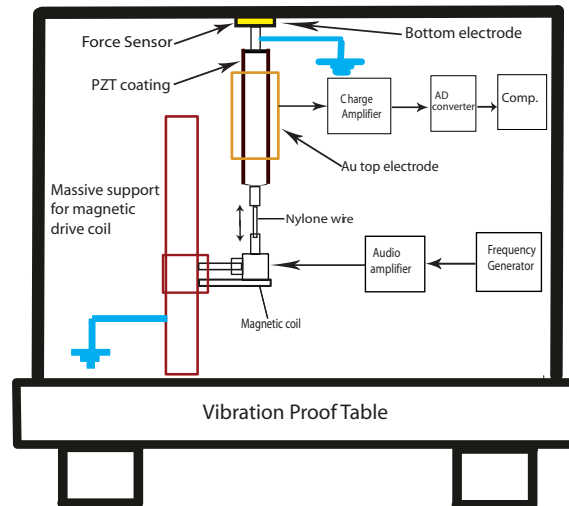
*Fig. 7.9:* Experimental setup to measure the piezoresponse from PZT coated steel fiber

## 7.7   Experimental setup for piezo−response measurement

Fig.7.9 shows the experimental setup for the piezo−response measurement of PZT coated fibers.  First, a vibration isolation table is used to isolate the noise from building vibrations.  An in−house built magnetic voice coil actuator is used to apply an oscillation force to the fiber .

The applied force is measured at the end of the PZT coated fiber.  The bottom electrode (steel fiber) and the whole set up was grounded to avoid any 50 Hz noise from surroundings. The Au coated top electrode was electrically connected to the charge amplifier which was connected to an analog digital converter.

Fig.7.10 (a-d) shows the actual setup to measure the induced charges from PZT coated steel fiber.  Two metal clips are used to connect top and bottom electrode.  To prevent an influence of surrounding noise, the whole
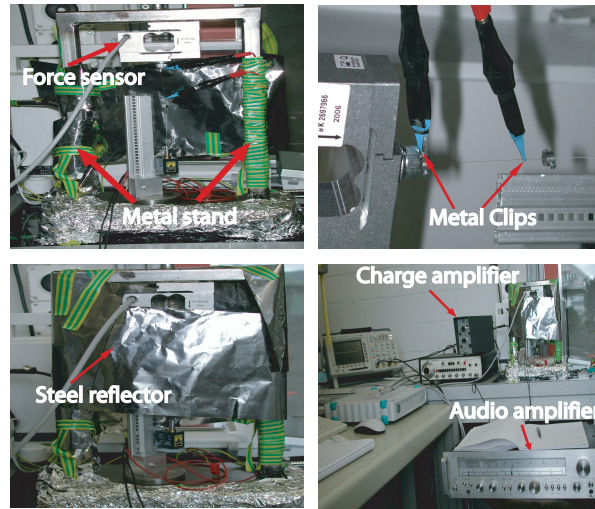
*Fig. 7.10:* Complete experimental set up for the piezoreponse measurements on fibers

set up is fully covered with metallic (steel) foil. In this way we are able to reduce 50 Hz noise to a value less than 6 mV.

## 7.8 Piezo−response of PZT coated fiber: Force Vs Output voltage

Fig.7.11 shows the applied force and measured piezoresponse voltage as a function of time for a 20Hz sinusoidal drive signal applied to the voice coil. In order to detect the sensitivity " S= U/F" of a fiber sensor, the quantity "U/F" was calculated for each part and the average and the standard deviation were determined .

We find that:

$$S = 1.95V/N = 1.95 \pm 0.175V/N \tag{7.1}$$

The relative length change $\Delta$ L/L of the sensor caused by an applied force
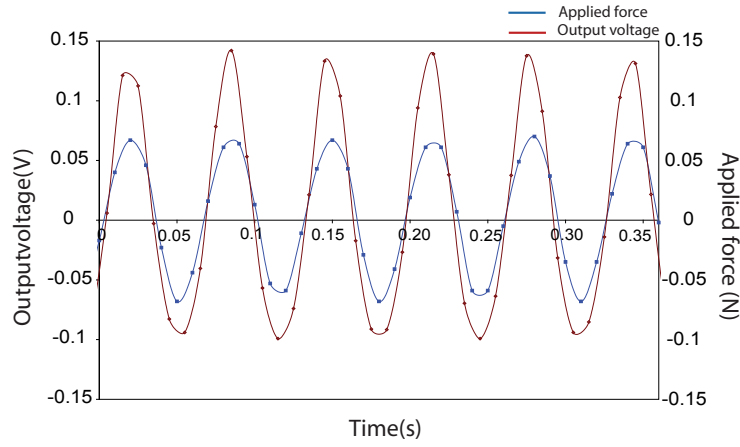
*Fig. 7.11:* Piezoresponse of PZT coated steel fiber at 20Hz

F can be calculated by

$$\Delta L/L = 1/E \times F/A \tag{7.2}$$

Where E is the elastic modulus of the steel fiber coupled by the PZT film, that is roughly equal to 85 GPa, A = $(\pi/4) \times d^2$ is the area of the steel fiber with d = 0.1mm.

The relative length change is given by

$$\Delta L/L = d_{31} \times U_{piezo}/d_{piezo} \tag{7.3}$$

where $d_{31}$ is the piezo material constant, $U_{piezo}$ is the voltage measured and d is the thickness of the PZT layer. From equation 7.2 and 7.3, piezoelectric coefficient can be calculated by following equation:

$$
\begin{aligned}
d_{31} &= F/(A_{fiber} \times E_{fiber}) \times (d_{piezo}/U_{piezo}) \\
&= (0.128N \times 4 \times 10^{-6})/(0.220 \times \pi \times (0.1mm)^2 \times 85GPa) \\
&= 870pm/V
\end{aligned}
$$

which is comparable to the value published by Tsuchiya et.al [120].

## *7.9 Summary*

Lead Zirconate Titanate (PZT) thin films have been successfully deposited on Au/glassfiber, Steel and Cu fiber. Deposition parameters are extremely important to get homogeneous poly−crystalline films. X−ray diffraction (XRD) reveals pervoskite structure formation on PZT coated fibers. All the coated fibers have (110) preferred crystallographic orientation. Some pyrochlore phase has been observed on coated fibers which are processed at higher temperature ($650^0$C) for longer duration (6min). Surface micro−structure shows dense and grainy structure on Au/glassfiber, steel, and Cu fiber. No micro cracks appear on PZT coated Au/glassfibers. Few micro−cracks have been observed on PZT coated steel and Cu fibers. This might be due to the difference in coefficient of thermal expansion between PZT and substrate. Chemical investigations have been performed by X−ray photoelectron spectroscopy (XPS) on all coated fibers. Atomic concentration of Pb, Zr, Ti and O are close to stoichiometric ratio in all coated fibers. Pb/Zr+Ti ratio of the fibers are in the range of 1.0 to 1.4, which is comparable to the target value (1.2).

A PZT coated steel fiber has been investigated as a force sensor. Sensor sensitivity of 1.95 V/N and a piezo material constant $d_{31} = 870$ pm/V have been found.

# 8

# Conclusion and outlook

A detailed study of a pulsed DC magnetron sputtering process of piezoelectric (PZT) thin films has been performed from single metallic PZT target. Si wafers and fibers have been used as substrate material for film deposition. Process parameters such as substrate temperature, $O_2$ partial pressure and annealing conditions (CA and RTA) have been investigated.

PZT films have been deposited on Ti/Pt/Ti coated Si wafers in the presence of different oxygen partial pressure within the plasma. First, films were deposited in low oxygen partial pressure. After post heat treatment by CA and RTA, XRD revealed the formation of pure pervoskite phase. CA and

RTA processed films lead to a different preferred crystallographic orientation (110 from CA and 111 from RTA). Annealed wafers show the dense and multi− crystalline structure. XPS results revealed that the atomic concentrations are in proportion and to the target values. Since XPS is sensitive to only few nm from the top layer, depth profiling has been performed by GDOES method. It has been found that the atomic concentration of Pb, Zr and Ti are close to the target value but only oxygen deficient perovskite has been obtained.

PZT films were further deposited with higher oxygen partial pressure within the plasma to overcome the oxygen deficiency in the samples. Fully oxidized PZT structure has been obtained after the CA and RTA treatments. Furthermore, hardness and Young's modulus of higher oxygen content films were almost three times higher than the oxygen deficient films. This is because of the higher number of defects site present in oxygen deficient film, which act like pinning centers and preventing the crystallization of PZT grains. Dense and multi−crystalline structures have been observed in all samples. Few micro−cracks have been observed, which are due to difference in thermal expansion coefficient of the PZT and substrates (Ti, Pt). Depth profiling by GDOES revealed that the atomic concentration of Pb, Zr, Ti and O are in stoichiometric ratio and close to the target value. Electrical properties of the oxygen enriched samples have been investigated by measuring hysteresis loops. CA processed films show higher polarization and remanence value compared to the RTA processed films because of larger grain sizes and different polarization axis. CA processed samples have 100 polarization axis, which is easy to polarize, while RTA treated samples have a hard polarization axis (110). Only minor loops (not completely saturated) have been obtained on these samples due to an instrumentation limit. Saturation polarizations

of CA and RTA processed films have been estimated from the minor loops by a newly developed method. In this method upward and downward slopes are plotted as a function of an electric field. A linear relationship has been obtained and extrapolated beyond the maximum applied electric field. Intersection point of upward and downward slope gives an estimated saturation polarization of the films.

After obtaining the optimized process parameters on wafers, PZT thin films have been deposited on fiber substrate. Some modification of process parameters were essential because of: different fiber geometry, substrate temperature and sticking of Ti atoms on fiber substrate. PZT thin films have been deposited on Au/Glassfiber, Steel and Cu fibers. It has been found the pure perovskite structure can be obtained at $650^0$C by RTA treatment. All RTA processed films show (110) preferred crystallographic orientation same as obtained on wafers (with high oxygen). A dense, homogeneous and multi−crystalline structure has been observed on all fibers. Some mirco−cracks have been appeared on Steel and Cu fibers, which are due to a large difference in the thermal expansion coefficient of PZT and the substrates. Atomic concentrations of Pb, Zr, Ti and O atoms are in stoichiometric ratio and close to the target value.

A PZT coated steel fiber has been investigated as a force sensor. Sensor sensitivity of 1.95 V/N and a piezoelectric coefficient, $d_{31} = 870$ pm/V has been found. The sensitivity and piezo material constant of PZT coated steel fiber sensor fabricated during this work is the highest ever reported for this type of device upto out best knowledge.

Thus, PZT films with pure pervoskite structure have been successfully obtained on wafers and fibers using a single metallic PZT target by reactive sputtering.

## 8.1  Outlook

It has been demonstrated the application of PZT coated fibers as a piezoresponsive sensor. Further investigations are necessary to understand the mechanism and influencing parameters, which are given as follows:

At a fundamental level, adhesion of Ti atoms on fibers have been a great problem, which deviates the perovskite structure to a Ti deficient phase. So, further experiments are an essential to control and to improve the sticking of Ti atoms on the fibers. The solution principally lies in substrate temperature and partial pressure of oxygen within the plasma.

In order to implement these PZT coated fiber sensor for industrial scale, sensitivity of these fibers has to be studied in detail. Sensitivity of the fibers can be varied with the different fiber lengths. As the elasticity and modulus of each fiber is different than others. Detailed study should be carried out on the sensitivity of the different coated fibers substrate such as Au/glassfiber, Ti/Pt/Ti coated glass fibers, Pt fibers, Cu fibers etc.

PZT coated fibers can be applied in a aviation industry. Hence, bending properties of fibers should be carried out in detail.

In order to obtain high piezo response, PZT coated fibers could be arranged in a structure like active fiber composites (AFC's) or Macro Fiber Composite (MFC).

The size and form factor of the composite should be determined to obtain the piezoelectric power output, if mechanical forces and frequencies are known. A prototype should be built for the application to ensure the success in a real-world environment.

With keep in mind the above mentioned points, PZT coated fibers can be applied for the following industrial application:

- PZT coated fibers can be used as energy harvesting sensors, where voltage can be produced from surrounding vibrations. This could be a great technological achievement to the areas where accessibility of electricity is restricted.

- In recent years, a great interest of active materials to integrate structurally into bendable or curved lightweight structures has been increased such as in integration of active materials into helicopter rotor blades. PZT coated fibers can be used as a bendable active structure, which can be implemented into rotor blades.

- PZT coated fibers can be used in telecommunication devices as a phase modulator, where piezoelectric coating is used to generate a stress, inducing a optical path length change in the fiber. In this way modulated signal traveling along the fiber can be controlled. In addition to the modulating the signals, piezoelectric coating can also be used to physically displace the fiber, so as to act like an actuator.

- PZT coated fibers can be used in sports industry, such as tennis or skiing. These self-powered PZT fibers actively dampen the vibration created during a ball strike or edge chatter from a ski turn and use the energy to create electrical force to control the shape of the ski or racket, using piezo properties to counteract the forces.

- PZT coated fibers can be used as a source to power networks of wireless sensors. PZT sensor can be attached to the support beams in a structure. As the structure gets under strain, the voltage created by the piezoelectric material stored up in a capacitor. Once the capacitor voltage reached a certain level, than the power can be transferred to a transmitter which sent a wireless signal to some receiver.

- PZT coated fibers can be used in structural health monitoring (SHM) area, where a high quality sensors is required.

This work can be concluded by the following quotation:

*I am enough of an artist to draw freely upon my imagination. Imagination is more important than knowledge. Knowledge is limited. Imagination encircles the world: Albert Einstein*

# Bibliography

[1] W.G. Cady. *Piezoelectricity.* Dover Publications, Inc., New York, 1964.

[2] K. Aizu. *Phys. Rev*, 146,:423, 1966.

[3] J. Fousek and V. Janovec. *J. Appl. Phys.*, 40,:135, 1969.

[4] L.E. Cross. *Thermodynamic phenomenology of ferroelectricity in single crystal and ceramic systems.* Physics of Electronic Ceramics Part B., Dekker, New York, 1972.

[5] J.F. Nye. *Physical Properties of Crystals.* Oxford University Press, Oxford, 1985.

[6] M. Lines and A. Glass. *Principles and Applications of Ferroelectrics and Related Devices, 87.* Clarendon Press, Oxford, 1977.

[7] B. Jaffe, W. R. Cooke Jr., and H. Jaffe. *Piezoelectric Ceramics.* Academic Press, New York, 1971.

[8] F. Jona and G. Shirane. *Ferroelectric crystal.* Dover Publications, Inc, New York, 1993.

[9] W. J. Merz. *Phys. Rev.*, 76:1221, 1949.

[10] S. Hoshino, Y. Mitsui, F. Jona, and R. Pepinsky. *Phys. Rev.*, 107:1255, 1957.

[11] B. T. Batthais and A. Von. Hippel. *Phys. Rev.*, 73:1378, 1948.

[12] L. L. Hench and J. K. West. *Principles of Electronic Ceramics.* Wiley-Interscience, 1990.

[13] B.Jaffe, W.Cook, and H.Jaffe. *Piezoelectric ceramics in non metallic solids, 3.* London, acedamic press, 1971.

[14] A. Safari, R. K. Panda, and V. F. Janas. In *Rutgers University, Piscataway NJ 08855, USA.*

[15] L. Tonks and I. Langmuir. *Phys. Rev.*, 34:876, 1929.

[16] A. Grill. *IEEE Press,Piscataway, NJ,*, 1994.

[17] S. Eliezer and Y. Eliezer. *The Fourth State of Matter.* Taylor & Francis; 2nd edition, 2001.

[18] F. F. Chen. *Introduction to Plasma Physics 2nd ed. New York,.* Springer, 1984.

[19] B. S. Tanenbaum. *Plasma Physics.* New York, NY: McGraw-Hill,, 1967.

[20] R. J. Goldston and P. H. Rutherford. *Introduction to Plasma Physics.* Philadelphia, PA: IOP Publishing,, 1995.

[21] P. C. Clemmow and J. P. Dougherty. *Electrodynamics of Particles and Plasmas.* New York, NY: Perseus Books, 1989.

[22] T. Maruyama and T. Morishita. *Applied Physics Letters*, 69(7):890, 1996.

[23] T. Unold, I. Sieber, and K. Ellmer. *Applied Physics Letters*, 88(21):213502, 2006.

[24] A. Gupta and A. D. Compaan. *Applied Physics Letters*, 85(4):684, 2004.

[25] C. S. Hwang, S. O. Park, H.J. Cho, C. S. Kang, H.K. Kang, S. I. Lee, and M. Y. Lee. *Applied Physics Letters*, 67(19):2819, 1995.

[26] S.O. Chung, J. W. Kim, G. H. Kim, C. O. Park, and W. J. Lee. *Japanese Journal Of Applied Physics Part 1*, 36(7A):4386, 1997.

[27] J.Hong, H.W. Song, S. Hong, H. Shin, and N. Kwangsoo. *Journal of Applied Physics*, 92(12):7434, 2002.

[28] S. Jaydeep, S. Yadav, B. P. Malla, A. R. Kulkarni, and N. Venkatramani. *Applied Physics Letters*, 81(20):3840, 2002.

[29] D.L. Smith. *Thin Film Deposition*. McGraw Hill, 1995.

[30] A Auciello and A.I.Kingon. In *proceeding of ISAF 92, IEEE eight international symposium on application of ferroelectrics,Greenville, SC, USA,*, 1992, 320.

[31] K. Sreenivas and M. Sayer. *Journal of Applied Physics*, 64, No. 3:1484, 1988.

[32] M. Kitagawa R. Takayama I. Kanno, S. Hayashi and T. Hirano. *Appl. Phys. Lett*, 66:145, (1995).

[33] S. Trolier-McKinstry K. Yamakawa and J.P. Dougherty. *Materials Letters*, 28:317, 1996.

[34] S. B. Krupanidhi and M. Sayer. *Journal of Vacuum Science & Technology A: Vacuum, Surfaces, and Films*, 2(2):303, 1984.

[35] A. I. Kingon, H.N.Al sharef, K.D. Gifford, T.M. Graettinger, S.H.Rou, P.D Hren, O.Auciello, and S.Bernacki. *Integrated ferroelectrics*, 2:361, 1992.

[36] A. Anders. *Surface and coating Technology*, 183:301, 2004.

[37] A. Belkind, A. Freilich, J. Lopez, Z. Zhao, W. Zhu, and K. Becker. *New Journal of Physics*, 7:90, 2005.

[38] S. Schiller, K. Goedicke, J. Reschke, V. Kirchhoff, S. Schneider, and F. Milde. *Surf. Coat. Technol.*, 61:331, 1993.

[39] L.B. Jonsson, T. Nyberg, I. Katardjiev, and S. Berg. *Thin Solid Films*, 365:43, 2000.

[40] J. Vlecek, A.D. Pajdarov, and J. Musil. *Contrib. Plasma Phys.*, 44, No. 5-6:426, 2004.

[41] S. M. Rossnagel, J. J. Cuomo, and W D Westwood. *Handbook of Plasma Processing Technology Park Ridge,*. NJ: Noyes Publications, 1990.

[42] A. Belkind, A. Freilich, and R.A. Scholl. *J. Vac. Sci. Technol. A*, 17:1934., 1999.

[43] D.E.N.Davies and S.Kingsley. *Electron. Letters*, 11:453, 1975.

[44] D. M. Costantini, H. G. Limberger, R. P. Salathe, C. A. P. Muller, P. Muralt, and N. Setter. *Applied Physics Letter*, 78, No. 15:2193, APRIL 2001.

[45] G. R. Fox, C. A. P. Muller, N. Setter, N. H. Ky, and H. G. Limberger. *Journal of Vacuum Science & Technology A: Vacuum, Surfaces, and Films*, 14,Issue 3:800, 1996.

[46] M.Sayer K.Sreenivas and Paul Garrett. *Thin solid films*, 172:251, 1989.

[47] J. Edmison, M. Jones, Z. Nakad, and T. Martin. In *Sixth International Symposium on Wearable Computers (ISWC 2002)*, October 2002, 41.

[48] See for example the lifeshirt system of vivometrics. http://www.vivometrics.com.

[49] http://www.gzespace.com/.

[50] P. Gould. *Materials Today*, page 38, October 2003.

[51] In *http://www.apple.com/pr/library/2003/jan/07burtonipod.html*.

[52] R.B. Cass. *Am. Ceram. Soc. Bull*, 70:424, 1991.

[53] S.Cai, C.E. Miller, L. Pedersen, O.T. Srensen, and Y. Xu. *Ferroelectrics*, 196:69, 1997.

[54] H.Sato, Y. Shimojo, and T. Sekiya. *proceeding of SPIE*, 5062:292, 2003.

[55] R.Thomas, S. Mochizuki, T.Mihara, and T.Ishida. *Materials Science and Engineering*, B95:36, 2002.

[56] E. Wu, K.C. Chen, and J.D. Mackenzie. *Mater. Res. Soc. Symp. Proc.*, 180:663, 1990.

[57] A. Bhalla. *ceramic transactions, ferroelectric films*, 25:73, 1992.

[58] A.T. Chien, X. Xu, J.H. Kim, J. Sachleben, J.S. Speck, and F.F. Lange. *J.Mater.Res.*, 2:339, 1993.

[59] K Miller and F Lange. *J.Mater. Res.*, 6:2387, 1991.

[60] M.Kumagai and G.Messing. *J Am, Ceram. Soc*, 67,11:c230, 1984.

[61] Choi D.-K. Nam H.-J. and Lee W.-J. *Thin Solid Films*, 371:264, 2000.

[62] C. Millon, C. Malhaire, C. Dubois, and D. Barbier. *Materials Science in Semiconductor Processing*, 5:243, 2002.

[63] Z. J. Wang, J. R. Chub, R. Maedac, and H.i Kokawaa. *Thin Solid Films*, 416:66, 2002.

[64] L. D. Madsen and L. Weaver. *J. electron. mater*, 21:93, 1992.

[65] T. Maeder, L. Sagalowicz, and P. Muralt. *Jpn. J. Appl. Phys.*, 37:2007, 1998.

[66] K. Abe, H.i Tomita, H.i Toyoda, M. Imai, and Y.i Yokote. *Jap, Jor.of applied physics*, 30 , 9B:2152, 1991.

[67] T. Maeder, P. Muralt, L. Sagalowicz, I. Reaney, M. Kohli, A. Kholkin, and N. Setter. *Appl. Phys. Lett.*, 68:776, 1996.

[68] K. Aoki, Y. Fukuda, K. Numata, and A. Nishimura. *Jpn. J. Appl. Phys.*, 1995:192, 34.

[69] J. S. Horwitz, K. S. Grabowski, D. B. Chrisey, and R. E. Leuchtner. *Applied Physics Letters*, 59, 13:1565, 1991.

[70] P. Verardi, M. Dinescu, F. Craciun, and V. Sandu. *Thin solid film*, 311:171, 1977.

[71] Charles Kittel. *Introduction to Solid State Physics*. Wiley; 7 edition, 1995.

[72] N. W. Ashcroft and N. D. Mermin. *Solid State Physics*. Brooks Cole, 1976.

[73] E. Meyer, H. J. Hug, and R. Bennewitz. *Scanning probe microscopy, The Lab on a Tip*. Springer, 2004.

[74] M.R. Winchester and R. Payling. *Spectrochim. Acta*, B59:607, 2004.

[75] R. Payling, D.G. Jones, and A. Bengtson. *Glow Discharge Optical Emission Spectrometry*. John Wiley and Sons: Chichester, 1997.

[76] W.C. Oliver and G.M. Pharr. *J. Mater. Res.*, 19:3, 2004.

[77] B. Joensson and S. Hogmark. *Thin Solid Films*, 114:257, 1984.

[78] P. Schwaller, A. Fischer, R. Thapliyal, M. Aeberhard, J. Michler, and H.J. Hug. *Surface & Coatings Technology*, 200:1566, 2005.

[79] C.V.R. Vasant Kumar, R.Pascual, and M.Sayer. *J. Appl. Phys*, 71(2):864, 1992.

[80] K.Y. Kim, S.T. Kim, and W.K. Choo. *Jpn. J. Appl. Phys.*, 32:1700, 1993.

[81] S. Hiboux and P. Muralt. *Ferroelectrics*, 224:743, 1999.

[82] C. Lee, S. Kawano, T. Itoh, and T. Suga. *J. Mater. Sci.*, 31:4559, 1996.

[83] J.F. Moulder, W.F. Stickle, P.E. Sobol, and K.D. Bomben. *Handbook of X-ray Photoelectron Spectroscopy.* Physical Electronics, USA, 1995.

[84] S.S. Dana, K. ETZOLD, and F. CLABES. *Jap.J. Appl. Phys.*, 69:4398, 1991.

[85] O. Sugiyama, Y. Kondo, H. Suzuki, and S.i Kaneko. *J. Sol-Gel Sci. Technol.*, 26:749, 2003.

[86] M.J. Bozack, J.R. Williams, J.M. Ferraro, Z.C. Feng, and R.E. Jones. *J. Electrochem. Soc.*, 142:485, 1995.

[87] C.R. Cho. *Cryst. Res. Technol.*, 35:77, 2000.

[88] A.R. Zomorrodian, A. Messarwi, and N.J. Wu. *Ceram. Int.*, 25:137, 1999.

[89] H.J. Sun, E.S. Choi, S.Y. Kweon, N.K. Kim, S.J. Yeom, J.S. Roh, and H.C. Sohn. *Jpn. J. Appl. Phys.*, 42:L1504, 2003.

[90] *American Piezo Ceramics,.* Mackeyville, PA.

[91] D.F. Bahr, J.S. Robach, J.S. Wright, L.F. Francis, and W.W. Gerberich. *Mater. Sci. Eng., A Struct. Mater. : Prop. Microstruct. Process.*, 259:126, 1999.

[92] P.H. Xiang, X.L. Dong, C.D. Feng, H. Chen, and Y.L. Wang. *Mater.Res. Bull.*, 38:1147, 2003.

[93] X.J. Zheng, Y.C. Zhou, and J.Y. Li. *Acta Mater*, 51:3985, 2003.

[94] T.H. Fang, S.R. Jian, and D. S. Chuu. *J. Phys.: Condens. Matter*, 15:5253, 2003.

[95] R.W. Rice, C.C. Wu, and F. Borchelt. *J. Am. Ceram. Soc.*, 77:2539, 1994.

[96] E.O.Hall. *Proc. Phys. Soc., Ser. B*, 64:747, 1951.

[97] J. N.J.Petch. *Iron and Steel Institute*, page 25, 1953.

[98] W. Huang, S.W. Jiang, Y.R. Li, Y. Zhang, and H.Z.Zeng. *Thin solid film*, 500:138, 2006.

[99] J.S.Cross, M.Fujiki, M.Tsukada, J.Kotaka, and J.Goto. *J. Mater.Res.*, 14:4366, 1999.

[100] I.Kanno, H.Koter, K.Wasa, T.Matsunaga, T.Kamada, and R.Takayama. *J.Appl. Phys.*, 93:4091, 2003.

[101] G. Velu and G. Remiens. *Microelectronics and Reliability*, 39(2):241, 1999.

[102] C. Legrand, T. Haccart, G. Velu, D. Chambonnet, L. Burgnies D. Remiens, F. Mehri, and J.C. Carru. *Microelectronics and Reliability*, 39 (2):251, 1999.

[103] A.C. Rastogi, S.R. Darvish, and P.K. Bhatnagar. *Materials Chemistry and Physics*, 73:135, 2002.

[104] P.Verardi, F.Craciun, L.Mirenghi, M.Dinescu, and V.Sandu. *Applied surface science*, 138:552, 1999.

[105] P. Delobelle, E. F. Blanc, and D.Remiens. *Thin Solid Films*, 515:1385, 2006.

[106] C.B.Sawyer and C.H.Tower. *Phys.Rev.*, 35:2691, 1983.

[107] K.P. Chong, S. C. Liu, and J. C. Li. *Intelligent structures,.* Elsevier applied science, London and New york, 2001.

[108] G. K. Haritos and A. V. Srinivasan. *Smart Structures and Materials*, 24:123, 1991.

[109] T.Honein, B. V. Honein, E. Honein, and G.Herrmann. *Journal of Intelligent Materials System and structures*, 6:229, 1995.

[110] J. W. Kim and J. G. Heinrich. *Journal of the Europian ceramic society*, 25:1637, 2005.

[111] G. R. Fox, C. A. P. Muller, N. Setter, N. H. Ky, and H. G. Limberger. *Journal of Vacuum Science & Technology A: Vacuum, Surfaces, and Films*, 14, Issue 3:800, 1996.

[112] W.Beckert, W.Kreher, W.Braue, and M.Ante. *Journal of the Europian ceramic society*, 21:1455, 2001.

[113] C.C. Chang and P.C. Lu. *Journal of Materials Processing Technology*, 95:128, 1999.

[114] W.L. Chang and J. L. He. *Journal of electro ceramics*, 13:47, 2004.

[115] M. G. Kang, K. T. Kim, and C. I.l Kim. *Thin solid films*, 448:398, 2001.

[116] N. Wakiya, K. Kuroyanagi, Y. Xuan, K. Shinozaki, and N. Mizutani. *Thin solid films*, 372:156, 2000.

[117] J. N. Kim, K. S. Kim, D. H. Kim, B. O. Park, N. K. Kim, and S. H. Cho. *Applied surface science*, 206:119, 2003.

[118] C. R. Cho. *Cryst. Res. Technol*, 35:77, 2000.

[119] W. Y. Choi, J. H. Ahn, and W. J. Lee. *Mater. Lett.*, 37(3):119, 1998.

[120] K. Tsuchiya, T. i Kitagawa, and E.i Nakamachi. *Precision engineering*, 27:258, 2003.

# Curriculum Vitae

**Name, surname**: Thapliyal, Ratnesh

**Date and place of birth**: September, 25. 1977, Karnprayag, India

**Nationality**: Indian

**Education:**

- 1985 - 1994: Primary and secondary central school, Karnprayag, Uttrakhand, India.

- 1995 - 1998: Bachelor of Science (B.Sc.) in Physics, Chemistry and Maths, Garhwal University, India

- 1998 - 2000: Master of Science (M.Sc) in Physics with solid state physics as a specialization, Indian Institute of Technology (IIT) Roorkee, India

- 2001 - 2003: Master of Technology (M.Tech) in Materials Science & Technology, Indian Institute of Technology (IIT) Bombay, India

- 2004 - 2007: Doctorate, Advance Fiber , Empa, Swiss Federal Laboratories for Materials Testing and Research - St Gallen & Philosophisch - Naturwissenschaftliche Fakult, University of Basel, Switzerland